Photon time-of-flight in tissue mimicking phantoms for the validation of a Monte Carlo software

Brian Angeli

Supervisors: Dr. Edouard Berrocal

Dr. Nina Reistad

Prof. Heidi Ottevaere (VUB)

Department of Physics

Lund University

This dissertation is submitted for the degree of

Master in engineering physics (Lund university)

European Master of Science in Photonics (VUB)

June 2019

Acknowledgements

I would like to thank Edouard Berrocal, my main supervisor and initiator of the topic of this master thesis. He guided me through the whole process, submitted guidelines for the experiments and helped me interpret them. He also pushed me to give the most out of myself and greatly helped me improve the structure and content of this thesis. I also want to show my gratitude toward Nina Reistad. She was the second supervisor and contributed to structure the experiments and lent a big part of her lab and tools for this project. She also helped improve my planning skills and gave me some tips and tricks for academic writing. Another person I want to praise here is professor Heidi Ottevaere who kindly accepted to be a supervisor for the Vrije Universiteit Brussel. She was also a helpful communication vessel between Lund Universoty and the Vrije Universiteit Brussel.

A person I certainly can't forget to mention here is Chen Xu, whom I did a large number of measurements with. He provided great support and excellent company in the lab. I also want to thank Birgitta Svenningsson who offered one of her week-end to help me with measurement. A big thank you to Hannes Jannson and Alexander Lundström for the help they provided as proofreaders. A big thank you to my parents as well, who supported me trough this long journey far from home. At last, I also want to acknowledge the T.I.M.E. organisation as well as the responsible persons at Lund and the VUB who made this exchange possible. It has been a wonderful time in Sweden and I would do it all again if able.

Abstract

The analysis of light propagation and characterisation of turbid media requires the use of modern simulation tools that are both powerful and reliable. One example of such tool is "Multi-Scattering", an open access, Monte Carlo based, simulation software running on Graphical Processing Units (GPU) cards. "Multi-Scattering" is provided for everyone via the following link: https://multi-scattering.com/.

This thesis focuses on validating the results from "Multi-Scattering" in the time domain using Photon Time-of-Flight Spectroscopy (PTOFS) on tissue mimicking phantoms. Those phantoms can reproduce in a controlled and accurate way the optical properties of tissues, namely the absorption and scattering coefficients. Thus they are important materials for the experimental validation of computational models simulating light propagation through tissues.

Indian ink and Intralipid are commonly used to make tissue mimicking phantoms. In order to know their optical characteristics, the absorption coefficient of Talens ink ($\mu_a = 9129$ cm^{-1} at 600 nm) and the scattering coefficient of intralipid ($\mu_s = 963$ cm^{-1} at 600 nm) have been measured using Collimated Transmission Spectroscopy (CTS). A large set of time pulses measured using PTOFS was compared with the corresponding simulated ones in order to inspect the variation in scattering, absorption and distance between the source and the receiving fibers. The simulation was also performed with different scattering phase functions in order to evaluate their impact on the simulation. The results are auspicious with good correlation between the simulated and experimental temporal responses.

Table of contents

Nomenclature

Symbols

μ_a Absorption coefficient

μ_s Scattering coefficient

μ_s' Reduced scattering coefficient

μ_t Attenuation coefficient

$\Phi(\hat{s}, \hat{s}')$ Scattering phase function

σ Cross section

τ Optical depth

θ Propagation angle

c Volumetric concentration

d Particle diameter

f Focal length

g Anisotropy factor

I Output intensity

I_0 Input intensity

L Fiber separation

l Traveling distance

$L(\vec{r}, \hat{s}, t)$ Light radiance

N Number of particles

n Particle density

n_p Refractive index of the particles

n_r Refractive index of the medium

r Radius

$S(\vec{r},\hat{s},t)$ Radiation of the source

V Volume

x Scattering parameter

Acronyms / Abbreviations

AOTF   Acousto-Optic Tunable Filter

APD   Avalanche Photo-Diode

CDF   Cumulative Density Function

CRD   Constant Fraction Discrimination

CTS   Collimated Transmission Spectroscopy

FWHM   Full Width at Half Maximum

GPU   Graphical Processing Unit

IRF   Instrumental Response Function

MC   Monte Carlo

NIR   Near InfraRed

PCF   Photonic Crystal Fiber

PDF   Probability Density Function

PSD   Particle Size Distribution

PTOFS   Photon Time-of-Flight Spectroscopy

RF   Radio Frequency

RTE   Radiative Transfer Equation

SNR   Signal to Noise Ratio

TCSPC   Time Correlated Single Photon Counting

VIS   VIsible Spectra

VOA   Variable Optical Attenuator

Chapter 1

Introduction

Today's medical world relies more and more on optical equipment and a significant amount of research is conducted in the development of laser-related diagnostics and treatment tools. As it often goes with research, more advanced techniques and complex methods are being invented and tested every year [1, 2]. This increase puts a higher demand on simulation software in order to accurately predict the effect of light interaction with biomedical materials since most problems cannot be analytically solved. As of today, multiple simulation tools already exist, relying on various approaches. Among those, the Monte Carlo simulation has gained more interest as the computational power largely increased over the past two decades. Good examples of what has already been done can be found in [3–5]. All these softwares have proven helpful to simulate simplified problems by making some assumptions. However, most of those assumptions are only valid in specific situations and hence, a new simulation tool is needed that covers a larger range of cases. What is presented and evaluated in this work are results from a new GPU based Monte Carlo code developed by J. Jönsson [6] and initiated by E. Berrocal [7]. This simulation tool works with as little assumptions as possible and can be found at:

https://multi-scattering.com/

This work mostly focuses on the response of a time pulse traveling trough tissues using time-of-flight measurements. Once the results of the code has been proven to match the experimental results with a good agreement, the model will be validated. Such validation work will allow the use of the Monte Carlo software for a variety of applications. For example, it will allow to generate look up tables for tissue characterisation and detection of different diseases. The look up table would, in our case, associate a given pulse shape with it's corresponding absorption and scattering coefficient. Photon interaction in tissues can also be analysed in detail in order to increase accuracy in laser radiation dosimetry. Many other applications could be mentioned, but this is not the focus of this work.

This report starts by explaining the general theory of light propagation through turbid media in chapter 2. The Monte Carlo tool is explained in chapter 3. In chapter 4 and chapter 5 the different methods involved when creating a sample are addressed, as well as the methods to measure its properties. In chapter 6 the results of both simulations and measurements are plotted and compared. In chapter 7 the results are discussed in order to draw conclusions on the reliability of the "Multi-Scattering" software.

Chapter 2

Theory

The simulation program was built to simulate photon transport through turbid media, such as biological tissues and tissue mimicking phantoms. Changes in refractive index due to particles or other optical non-uniformity are responsible for scattering of light in a material. Furthermore, materials absorb light at certain wavelengths. It is therefore important to understand the effects of both scattering and absorption in turbid media. In the next sections, the attenuation, absorption and scattering coefficients are defined, the scattering phase function will be detailed and the Radiative Transfer Equation (RTE) is introduced.

2.1   Attenuation, absorption and scattering coefficients

The optical properties of turbid media include the so called attenuation coefficient μ_t. This parameter can be used in the Beer-Lambert law.

$$I = I_0 e^{-\mu_t l} \qquad \text{where} \qquad \mu_t = n\sigma_t \qquad \text{and} \qquad n = \frac{N}{V} \qquad (2.1)$$

The Beer-Lambert law shows how the input intensity I_0 of a light source transits in a medium of length l with attenuation coefficient μ_t. I is the intensity of the transmitted light Equation 2.1 also shows the relation of μ_t with the particle density n, the attenuation cross section σ_t, N the number of particles with this cross section and the volume V. The optical depth $\tau = \mu_t l$ is also introduced here. An illustration of the Beer-Lambert law is showed in figure 2.1. In this illustration we can see that some light does not interact with the medium. This light is called direct light was measured in the work presented in chapter 4.
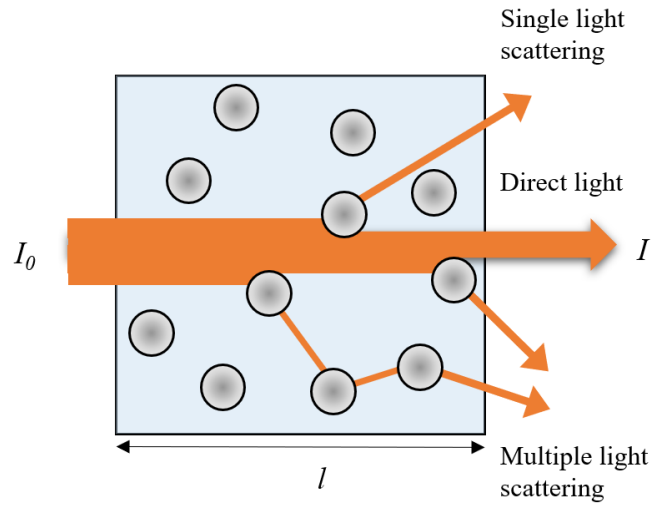
Figure 2.1 Illustration of light travelling through a turbid medium.

The attenuation coefficient is further developed in equation 2.2 as being the sum of the absorption coefficient μ_a and the scattering coefficient μ_s.

$$\mu_t = \mu_a + \mu_s \tag{2.2}$$

Figure 2.2 shows examples of 6 of the most frequent cases that can occur, where either scattering or absorption can be the dominant process in a given turbid medium.
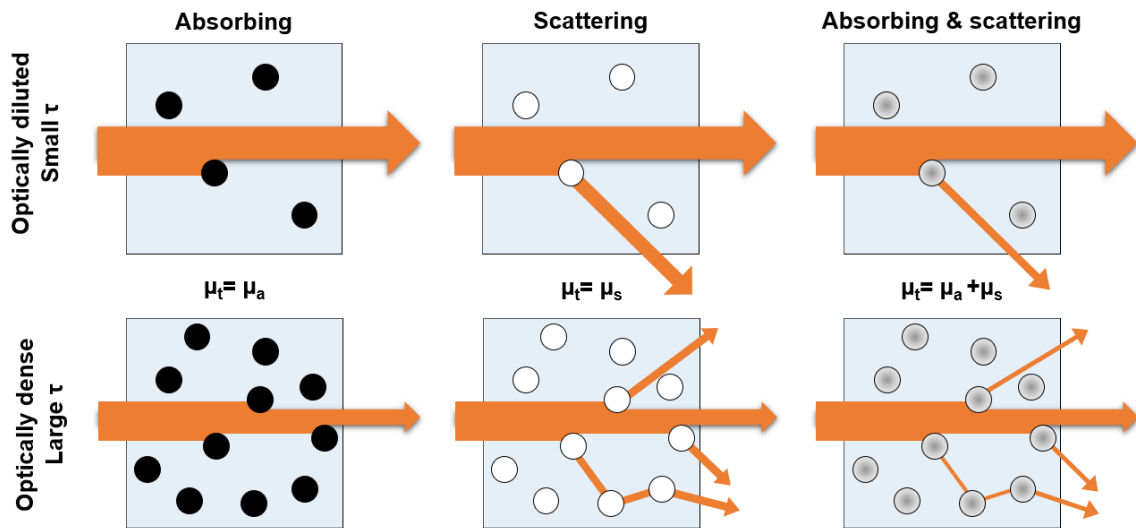

Figure 2.2 Representation of different turbid media. From left to right, a perfectly absorbing, perfectly scattering and a mixed medium is displayed. In the first row, the dilution is such that only one interaction occurs. In the second row, multiple scattering can also occur.

The reduced scattering coefficient μ'_s is introduced in equation 2.3 as

$$\mu'_s = \mu_s(1-g),\tag{2.3}$$

with g being the anisotropy factor, defined as [8]

$$g = \int_{4\pi}(\hat{s}\cdot\hat{s}')\Phi(\hat{s},\hat{s}')d\Omega = \langle\cos(\theta)\rangle,\tag{2.4}$$

with the scattering phase function $\Phi(\hat{s},\hat{s}')$, $\langle\cos(\theta)\rangle$ being the average of $\cos(\theta)$ and θ being the propagation angle. It can take any number between -1 (purely backwards propagation) and 1 (purely forward propagation). $g=0$ means a isotropic scatterer. In biological tissue, g is mostly situated between 0.8-0.98, with some exceptions [9].

2.2   Scattering phase function

The scattering phase function is the 3D angular phase distribution of light intensity scattered by a particle of certain size at a certain wavelength. It gives the probability for a photon to be scattered from its incident direction to another direction, with solid angle θ_s. When assuming spherical symmetry, the scattering phase function can be represented in 2D. Therefore all the plots in this section are rendered in 2D.

The scattering phase function can be calculated using either the Rayleigh approximation, the Henyey-Greenstein (HG) equation, or the Lorenz-Mie theory as explained and discussed below. In order to help us in this discussion, the scattering parameter x

$$x = \frac{\pi d}{\lambda}\tag{2.5}$$

is introduced as a useful tool to sort of the ratio between the particle diameter d and the wavelength of light λ.

Rayleigh approximation

The Rayleigh approximation gives valuable results when $x < 0.1$ (particle size <1/10 of the wavelength). Under such conditions the intensity for unpolarized light can then be calculated with the formula [10]:

$$I = I_0\frac{1+\cos^2\theta}{2R^2}(\frac{2\pi}{\lambda})^4(\frac{n_p^2-1}{n_p^2+2})^2(\frac{d}{2})^6\tag{2.6}$$

With R the distance to the particle and n_p the refractive index of the particle. An example of Rayleigh scattering for different particle sizes is shown in figure 2.3a. In the figure, the angles are relative to the propagation direction, hence 0° corresponds to propagation in the forward direction.
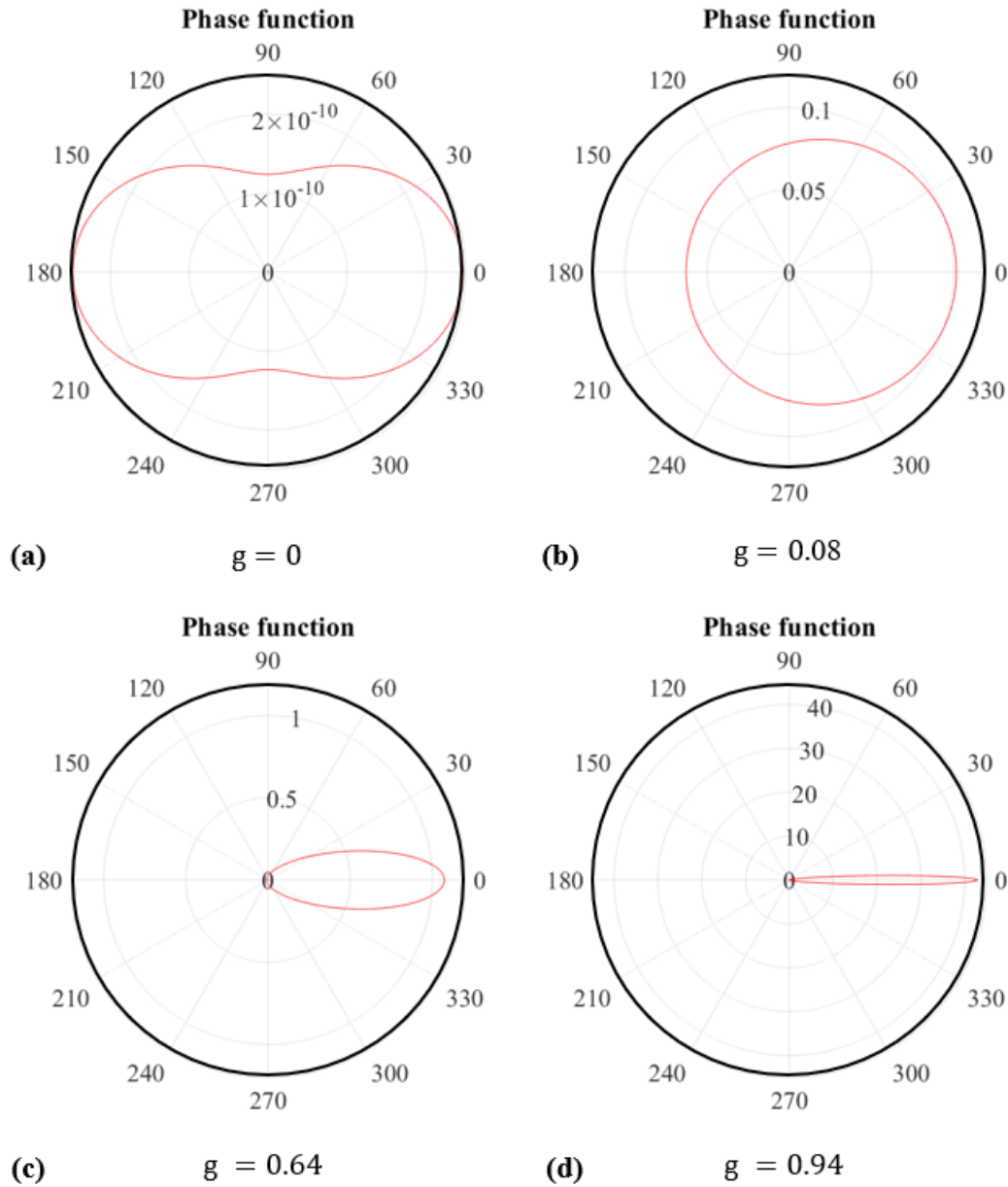

Figure 2.3 (a) The phase function for Rayleigh scattering with $R = 100$ nm, $d = 10$ nm, $n_p = 1.362$, $\lambda = 600$ nm. **(b)-(d)** Are examples of Henyey-Greenstein phase functions for various g.

Henyey-Greenstein

The Henyey-Greenstein phase function is an approximation that uses the anisotropy factor g. It is defined in [11] as

$$\Phi(\theta) = \frac{1}{4\pi} \frac{1-g^2}{[1+g^2-2g\cos(\theta)]^{3/2}} \tag{2.7}$$

An example for different g values is showed in figure 2.3. The g values were chosen to match the ones in figure 2.4 for better comparison.

Lorenz-Mie theory

The Lorenz-Mie scattering, later referred in this thesis as Mie scattering, assumes that the scatterer has a spherical shape and is illuminated with a plane wave. It is usually used when the particle size is comparable or larger than the wavelength of the incident light ($x > 0.1$). The solution is calculated with Bessel functions and Legendre polynomials and will not be detailed here. Further reading for the passionate reader can be found in [12] and [13]. What is important to note from the theory is that the scattering phase function depends on the wavelength of the light, the particle size, the refractive index of the particles and the refractive index of the surrounding medium n_r. Examples of Mie distributions are shown in figure 2.4 and 2.5. The intensity scale is relative compared to the maximum intensity and is plotted both in a linear scale (left) and a logarithmic scale (right). In figure 2.4 and 2.5 the particle size is changed and the refractive index of the scattering medium is kept constant. Another example is shown in appendix A where the particle size is kept constant and the refractive index is changed. From the figures, the trend is clear that photons are more likely to propagate in the forward direction for larger particle diameter. We can also see in figure 2.5 that a ripple pattern appears for larger particles. These ripples are not recreated by the Heyney-Greenstein, which is why this theory should be used with caution and avoided for particles with diameter exceeding 1 μm.
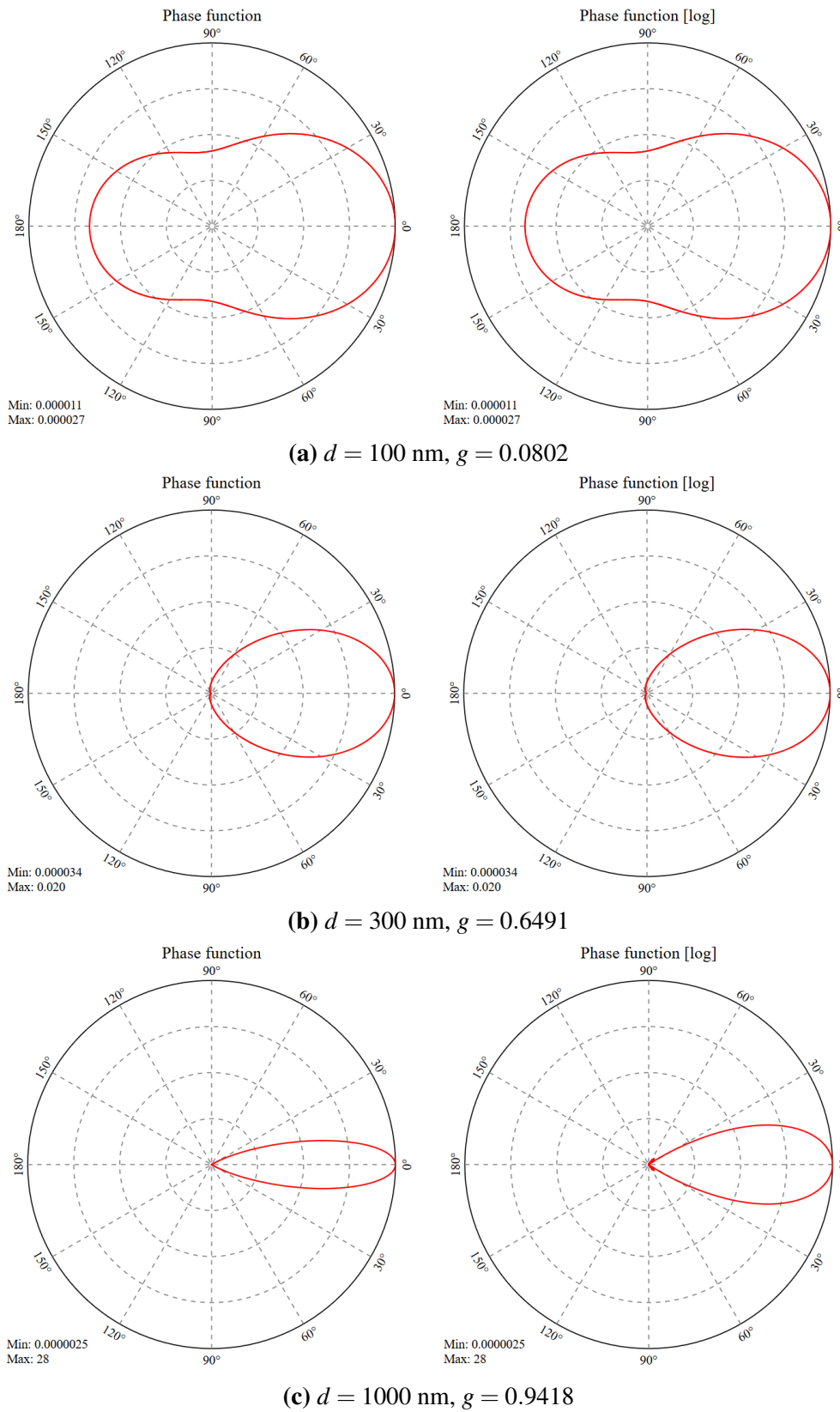
(a) $d = 100$ nm, $g = 0.0802$

(b) $d = 300$ nm, $g = 0.6491$

(c) $d = 1000$ nm, $g = 0.9418$

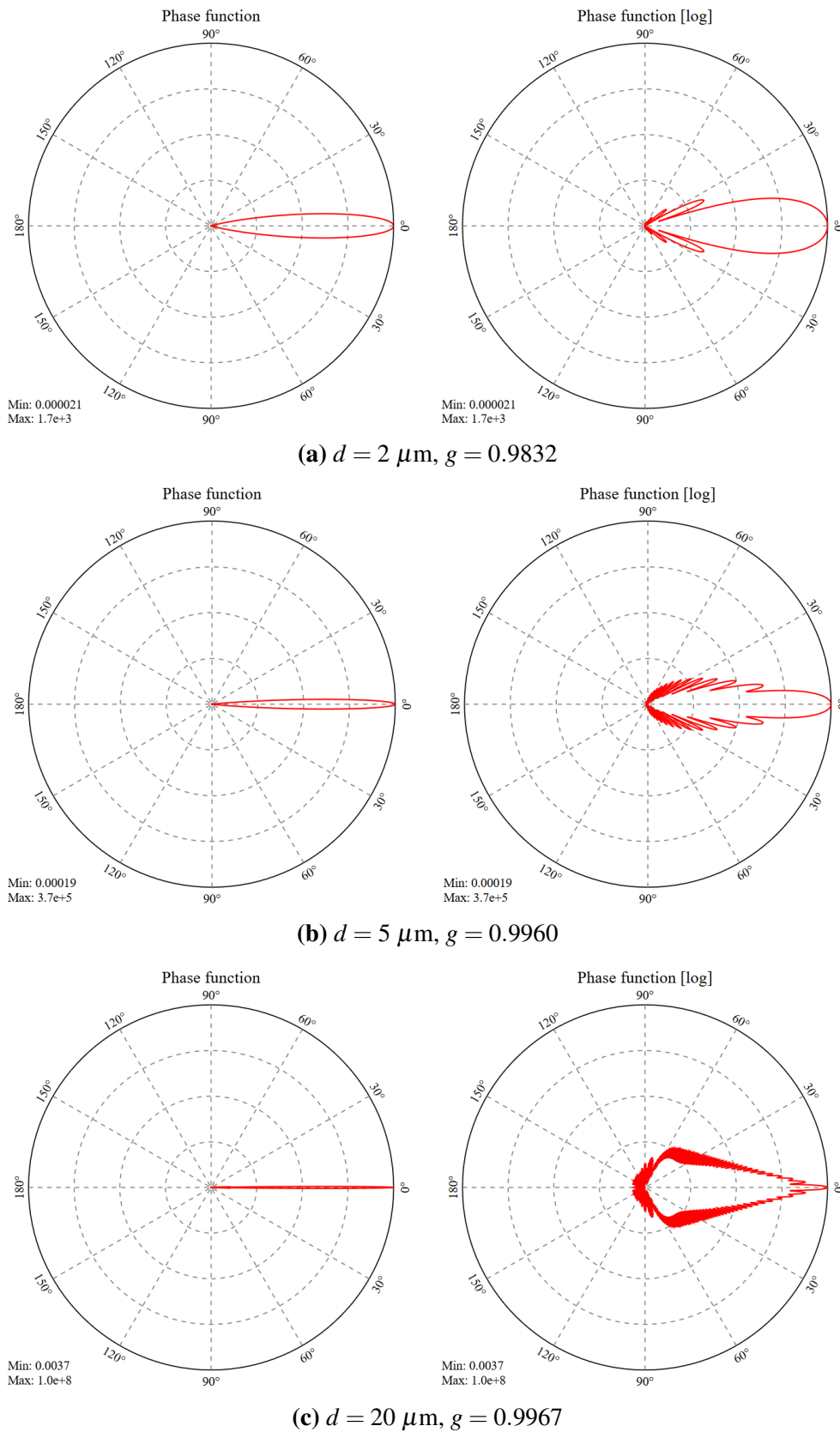**Figure 2.4** Examples of computed Mie scattering phase functions, for various particle diameters. Images created using the website: https://multi-scattering.com/. The linear plots are on the left, the log scale plots are on the right. $\lambda = 600$ nm, $n_p = 1.362$ and $n_r = 1.3315$.

Phase function

Min: 0.000021
Max: 1.7e+3

Phase function [log]

Min: 0.000021
Max: 1.7e+3

(a) $d = 2 \ \mu\text{m}$, $g = 0.9832$

Phase function

Min: 0.00019
Max: 3.7e+5

Phase function [log]

Min: 0.00019
Max: 3.7e+5

(b) $d = 5 \ \mu\text{m}$, $g = 0.9960$

Phase function

Min: 0.0037
Max: 1.0e+8

Phase function [log]

Min: 0.0037
Max: 1.0e+8

(c) $d = 20 \ \mu\text{m}$, $g = 0.9967$

Figure 2.5 Examples of computed Mie scattering phase functions, for various particle diameters. Images created using the website: https://multi-scattering.com/. The linear plots are on the left, the log scale plots are on the right. $\lambda = 600$ nm, $n_p = 1.362$ and $n_r = 1.3315$.

.

2.3   The Radiative Transfer Equation

FThe best way to represent light propagation in turbid media is by using the Radiative Transfer Equation (RTE). This equation is defined as

$$\frac{1}{v}\frac{dL(\vec{r},\hat{s},t)}{dt} = -\mu_s L(\vec{r},\hat{s},t) - \mu_a L(\vec{r},\hat{s},t) + \mu_s \int \Phi(\hat{s},\hat{s}')L(\vec{r},\hat{s},t)d\Omega' \qquad (2.8)$$
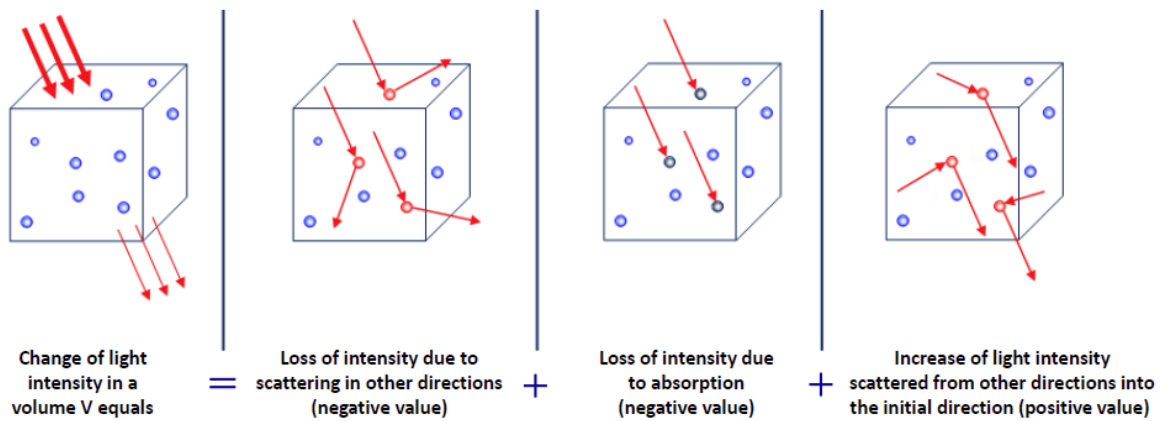

| Change of light intensity in a volume V equals | = | Loss of intensity due to scattering in other directions (negative value) | + | Loss of intensity due to absorption (negative value) | + | Increase of light intensity scattered from other directions into the initial direction (positive value) |

Figure 2.6 Graphical representation of the RTE, adapted from reference [7].

The radiance of light is noted $L(\vec{r},\hat{s},t)$ and describes the propagation of photon energy in the direction $\hat{s}$ at a position $\vec{r}$ and time t in an infinitesimal volume. The drawback of the RTE is that it cannot be solved analytically for cases of light transport through realistic scattering volumes, such as tissues. Therefore, computer algorithms based on the Monte Carlo method are used to solve the equation.

In this chapter the basic theoretical concepts of attenuation, absorption, scattering and the scattering phase function have been explained and combined into the RTE. An introduction to Monte Carlo simulation and how it tries to solve the RTE is given in chapter 3. A brief explanation of the "Multi-Scattering" software can also be found in that that chapter.

Chapter 3

Monte Carlo simulation

The Monte Carlo method is a broad term that designates computational algorithms that have a purely statistical approach to simulate complex problems. This statistical approach is looped numerous times in order to have a converging solution. Monte Carlo simulation can be used for various cases. It is for example used when the deterministic equation of a problem is too complex to be solved analytically, and is instead solved by repeated random sampling. Monte Carlo is commonly used in numerical integration, optimisation problems and creating illustrations of probability densities. In this work we use the latter application. Despite its effectiveness, the algorithm was not very popular in optics until the late 90's. This is explained by the great computational resources that accompanies the simulation. Nowadays computers have very high computational power and possibilities for parallel processing exists, which can reduce the computational time by several orders of magnitude. Therefore, the number of applications of the algorithm in the field of Bio-medical optics (and other sectors) has increased significantly. Efficient parallel processing is made possible thanks to graphical cards that can do a high amount of simple mathematical tasks in parallel. This leads us to the simulation tool that is described in this chapter.

3.1 General description

The aim of the Monte Carlo method is to solve a complex problem by breaking it down into (several) statistical problems with known Probability Density Function (PDF). The statistical problem is then fully solved for one random case and the procedure is repeated again for a very large set of cases in order to have good precision. Typically, the accuracy of the simulation improves with the square root of the amount of photons [8] where the simulation time increases linearly with this amount. This can be understood if we make the parallel with the standard deviation, which decreases with the square root of the population increase.

In order to have the correct probability for the scattering distances and angles, the program chooses a number randomly from a uniform Probability Density Function (PDF). This value is then associated with the value on its Cumulative Density Function (CDF). This value is associated with the CDF of the desired function and that corresponds to a final value in the PDF of that function. It is this last value that the program uses to do further calculations. An example of whole process is given in figure 3.1.
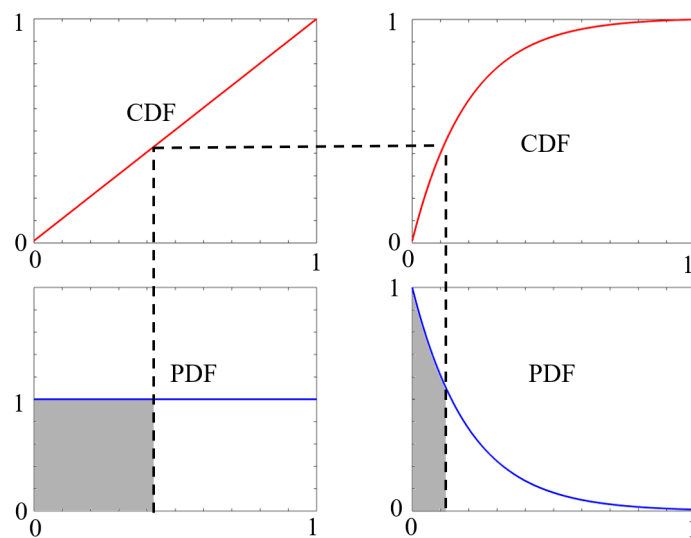
Figure 3.1 Schematic representation of the process of choosing a random value from any PDF. Starting from a random variable in a uniform PDF, bottom left, the corresponding CDF value, top left, is associated with the CDF of the desired function, top right, and the correct Monte Carlo value can be found in the desired PDF, bottom right.

3.2   "Multi-scattering" a GPU-based MC simulation

The program aims to solve the RTE numerically by using the Monte Carlo approach for a very large number of photons. A brief explanation of the algorithm and the assumptions that it uses is given here, further reading on the program can be found in [6], [7] and most recently [14]. The main assumptions that the software makes are listed below.

- Spherical particles

- Independent scattering, or that the scattering of light in a particle does not depend on the previous scattering result

- Unpolarized light source

- Random positioning of scatterering centres

The algorithm works on a homogeneous cube. Various input parameters can be given on the size of the cube, composition of the medium and properties of the laser beam. A start position is also decided for the center of the beam as well as the number of simulated photons. When all the input parameters have been set, the code can be started. The algorithm is summarized in figure 3.2. It starts by assigning several identical threads to the GPU, that is able to process these threads in parallel. Each thread is the simulation of a possible path a photon can take. Once a thread is finished, a new one is assigned immediately, in order to simulate the required amount of photons. The flowchart explains that the photon does multiple inquiries for scattering until it exits the scattering media. The PDF to determine the distance between 2 scattering events is the Beer-Lambert law of equation 2.1. If this distance is larger then the distance to exit the medium, no scattering happens and the exit protocol is applied. If the photon does scatter, the scattering angle is determined statistically with the scattering phase function.
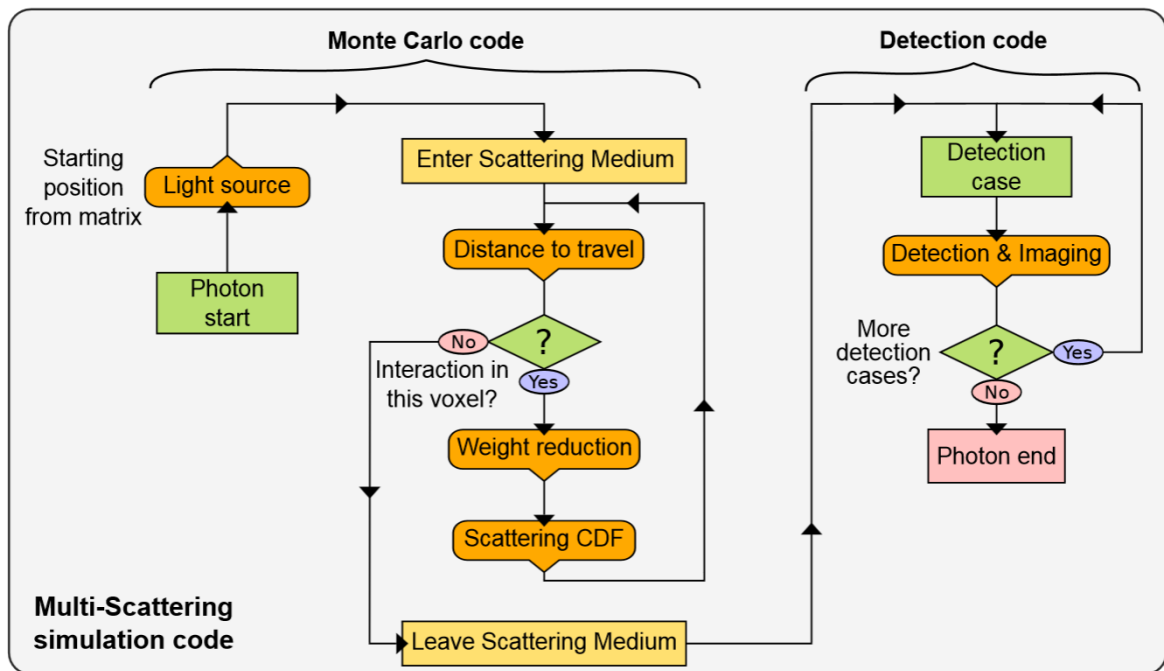
Figure 3.2 Flowchart of the Monte Carlo simulation and detection, figure taken from [14] with permission.

The approach that is chosen here for absorption is to give the photon a weight factor that scales with its path-length via the Beer-Lambert law. The weight factor is conserved when the photon exits the medium and is taken into account in the intensity plots. When the photon exits the medium, it is saved into various image matrices for each side of the cube. Currently the software outputs 4 different spatial images, as can be seen in figure 3.3.
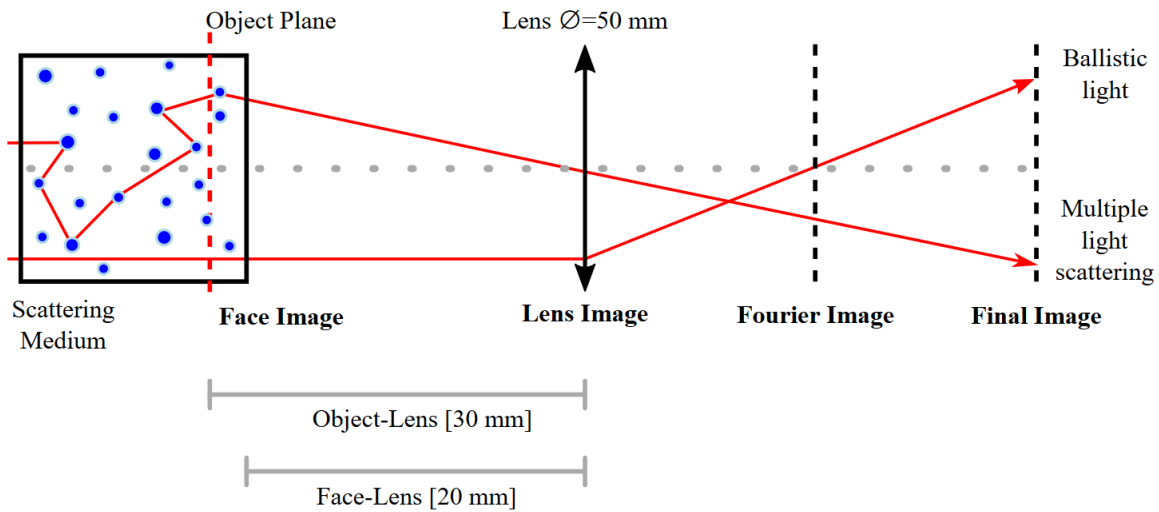
Figure 3.3 Schematic representation of the Monte Carlo simulation cube on the left side and the different output images on the right. Image taken from https://multi-scattering.com/.

These images are

- Face image: Shows the distribution of photons directly at a surface of the cube.

- Lens image: Shows the distribution of photons on a lens with focal length f and distance L from the input face of the cube. f and L can be chosen by the experimenter.

- Fourier image: Shows the distribution of photons in the Fourier plane, created by the previously mentioned lens.

- The final image: Shows the distribution of photons in the plane optically aligned with the lens.

In each of these images the corresponding photon time-of-flight is calculated and put into a histogram with 1 ps bin. The temporal response of the face image is studied in chapter 6.

Chapter 4

Collimated Transmission Spectroscopy

Collimated transmission measurements are used to measure the attenuation coefficient of a medium. When using a broadband light source, the attenuation, which is wavelength dependent, can be determined for a large spectral range. In this work, Indian ink from the brand Talens and Intralipid 20% from Fresenius Kabi are used to make tissue mimicking phantoms when mixed together with water. These materials are generally used for the making of tissue mimicking phantoms because of their optical properties, their cost and their ease of quickly producing robust samples [15, 16]. Mixed together and diluted in water, a sample can be achieved with any desired μ_s and μ_a. The Collimated Transmission Spectroscopy (CTS) method will be used to determine the attenuation coefficient of Indian ink and Intralipid 20% over a large range of wavelengths. These results will then be compared with the results from other papers and discussed. The aim of this chapter is to obtain reliable input parameters for the Monte Carlo simulation.

4.1   Setup and Method

The setup used for this experiment is shown in figure 4.1. A continuous beam of light enters an optical fiber and is collimated via a spherical lens located in front of the cuvette, filled with the fluid under investigation. At the other end of the cuvette the light is collected via another spherical lens, guided through a fiber and sent to two different spectrometers. A tungsten halogen light source (HL-2000-FHSA), which emits 7 W of light ranging from 360 nm to 2400 nm, was used and equipped with an attenuator TTL shutter. The optical fibers are multi-mode fiber (Thorlabs M41L02) with a diameter of 600 μm. The cuvettes were put in a temperature controlled cuvette holder (QPOD 2e), where a temperature of 20 °C was chosen to perform measurements. The cuvette sat in the middle of the holder and light enters through a 4 mm attenuation slit and exits it through a 2 mm slit. The 2 mm slit was positioned

exactly in the Fourier plane and ensures that only the collimated light enters in the fiber. For the visible range an OceanOptics QE65000 spectrometer was used. The spectrometer has a wavelength range going from 200 nm to 1100 nm, a bandwidth of 6 nm and an integration time of 10ms. For the near infrared range an Ocean Optics NIRQuest512 spectrometer with wavelength range going from 900 nm to 1700 nm, a bandwidth of 3 nm and an integration time of 8 s was used.
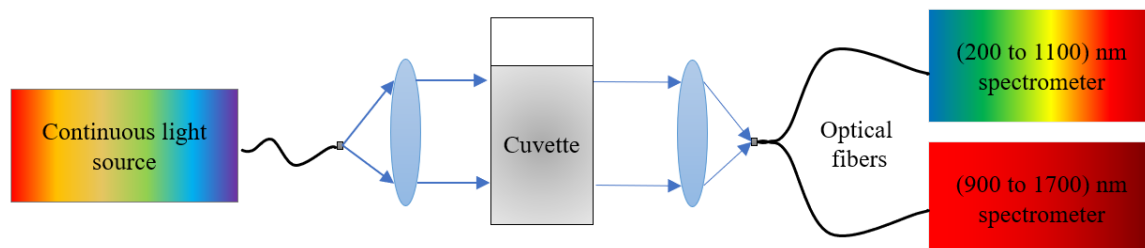

Figure 4.1 Setup for the collimated transmission spectroscopy using ocean optics spectrometers.

In order to find the attenuation coefficient of ink or intralipid, the intensity of two samples were measured. The first was a reference water measurement with intensity I_w. The other was a fluid measurement with intensity I. Both intensities can be represented using the Beer-Lambert law of equation 2.1.

$$I_w = I_0 e^{-\mu_w l} \qquad \text{and} \qquad I = I_0 e^{-\mu l} \qquad (4.1)$$

To make this measurement, de-ionized water with attenuation coefficient μ_w was used and put in the cuvette. The choice of water as a reference been made because it is important that the refractive index inside the cuvette n_r is the same in the reference and in the measurement. This way, the reflection from the cuvette is taken into account and will not interfere in the measurement. The fluid is a diluted amount of ink or intralipid that was added in the water cuvette. When the collimated light goes through the cuvette, part of it will be absorbed, part of it will be scattered and part of it will not interact. Only the light that does not interact is assumed to reach the detector. That light will be compared to the reference light and the attenuation coefficient can be extracted from equation 4.1 by dividing the two expressions, which gives the relative intensity ratio $\frac{I}{I_w} = e^{(-\mu+\mu_w)l}$. We can now extract μ

$$\mu = \frac{-ln(\frac{I}{I_w})}{l} + \mu_w. \tag{4.2}$$

Since the ink and the intralipid are diluted with volumetric concentration c we have $\mu = c\mu_t + (1-c)\mu_w$. From this and equation 4.2, we can determine the attenuation coefficient of the ink or intralipid.

$$\mu_t = \frac{-ln(\frac{I}{I_w})}{cl} + \mu_w \tag{4.3}$$

In order to determine μ_w, information has been retrieved from [17] and [18]. The data is plotted in figure 4.2. It is further assumed that $\mu_w = \mu_a$ since the scattering coefficient of de-ionized water is negligible.
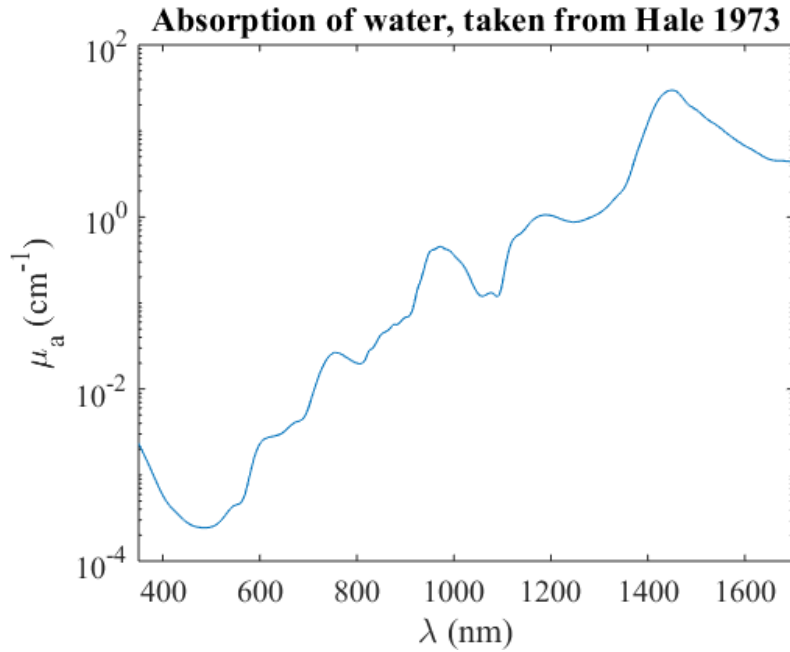
Figure 4.2 Absorption coefficient of water, as reported in [17].

4.2   Results and discussion

4.2.1   Ink solutions

In order to perform the measurement several diluted ink batches were made and measured. Those batches have a 1:100 or 1:200 ink to water ratio. They were then pipetted in ten steps of 0.02 ml in a cuvette with 3 ml water. The different cuvettes of a series can be seen in figure 4.3.
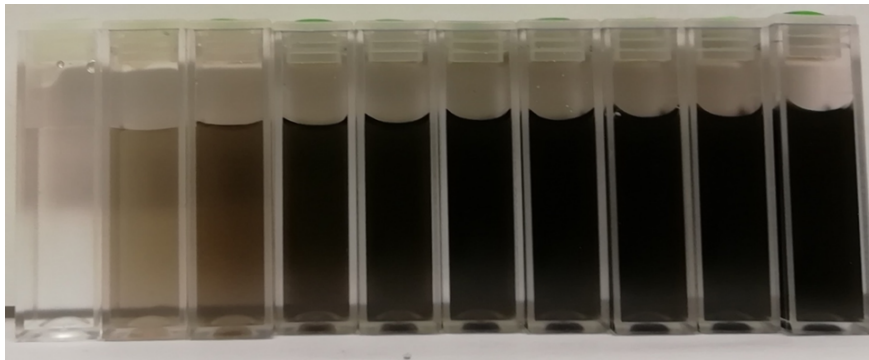
Figure 4.3 Example of cuvette series containing aqueous solution of ink, used for the determination of the absorption coefficient.

μ_t for all cuvettes of one series is showed as a function of wavelength in figure 4.4.
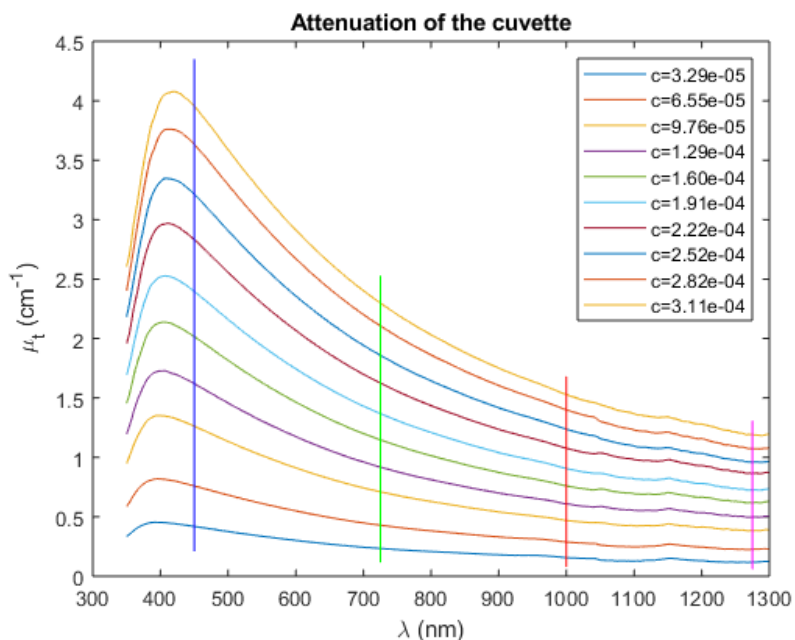
Figure 4.4 Attenuation coefficient in the cuvette for various wavelength and different ink concentrations.

Water has a strong absorption of water starting from 1300 nm, as can be seen in figure 4.2. Because of this, the results are poor for the measured signal above that wavelength and are therefore not shown in this work.

An interesting observation from figure 4.4 is the fact that the attenuation of the cuvette increases with ink concentration. In theory, this relation should be linear, since the attenuation depends linearly on the concentration. In order to verify this, the wavelengths 450 nm, 725 nm, 1000 nm and 1275 nm were chosen to make a linear analysis. The linear fit has another purpose, it can later be used to calculate the amount of ink needed for a desired attenuation in a sample. This is because the linear fit portrays the equation $\mu_a = aV$. Where a is the absorption per volume and V is the volume. The fit as well as the collected data points are shown in figure 4.5. As can be seen, the fits are really good ($R^2 > 99.8\%$) which suggest a correct measurement.
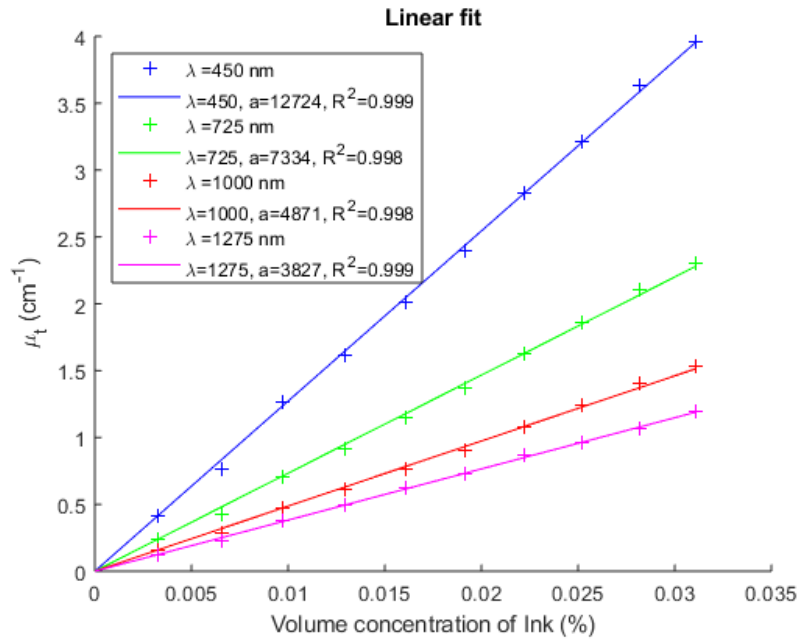
Figure 4.5 Attenuation coefficient of the cuvette mix compared to the concentration of Indian ink, for various wavelengths.

In figure 4.6, the attenuation coefficient of the ink is calculated for every wavelength using equation 4.3 and averaged out over the batches.
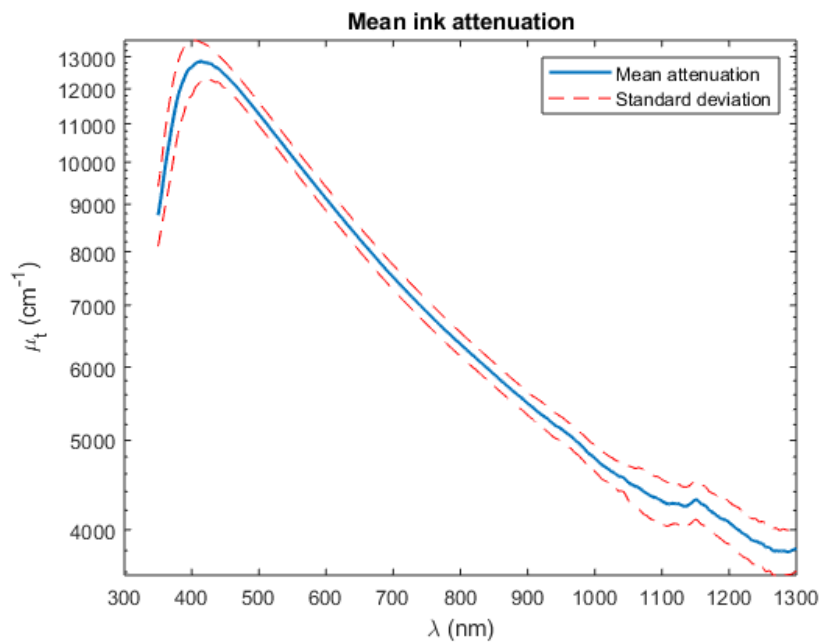
Figure 4.6 Average attenuation coefficient of Indian ink, compared to wavelengths.

Although no data has been collected for this particular ink brand, the final result was compared with literature references [15], and falls within the range of what is already measured. The reference also mentions that the absorption coefficient for ink is much higher than its scattering coefficient. In order to facilitate the making of the tissue mimicking samples in section 5.1.2 we will make the assumption that ink is a purely absorbing medium, or in other words that $\mu_a = \mu_t$.

4.2.2 Intralipids solutions

The same experiment has been performed on intralipid 20%. Several batches with a 1:5 ratio of intralipid were made. These batches were added in fifteen steps of 0.02 ml with a pipette in 3ml of de-ionized water. Figure 4.7 shows one series of cuvettes and the evolution of the intralipid density in the cuvettes.
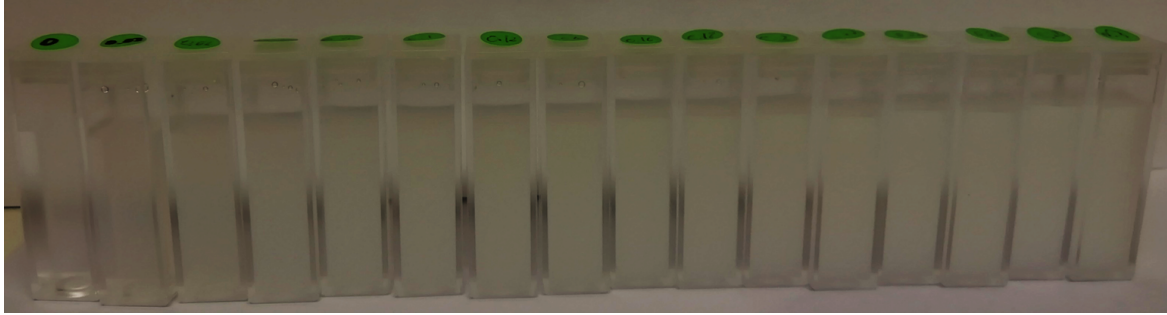

Figure 4.7 Example of cuvette series containing aqueous solution of intralipid, used for the determination of the scattering coefficient.

The attenuation of the whole cuvette is showed as a function of wavelengths in figure 4.8. The same comment can be made as for the ink regarding the signal beyond 1300 nm. It was therefore decided to remove the high wavelengths as well. Another notable item is that the Signal to Noise Ratio (SNR) is very poor below 500 nm for the samples with the highest concentration. This was even more pronounced in the last seven cuvettes in this region. Those cuvettes were therefore removed from the calculations and plots. The linear analysis for wavelengths 450 nm, 725 nm, 1000 nm and 1275 nm is plotted in figure 4.9. It is seen from the figure that the measurements done around 450 nm have a poor linear fit. It is especially visible in the figure since the fit was done using only the first two points to highlight the effect. The non linearity is probably due to photons scattering an additional time due to a too concentrated solution. Low SNR can also be mentioned as an additional reason for the highest concentrations. The fit for 1275 nm is not perfect either. For the other wavelengths, the fits are very convincing with $R^2 > 99\%$.
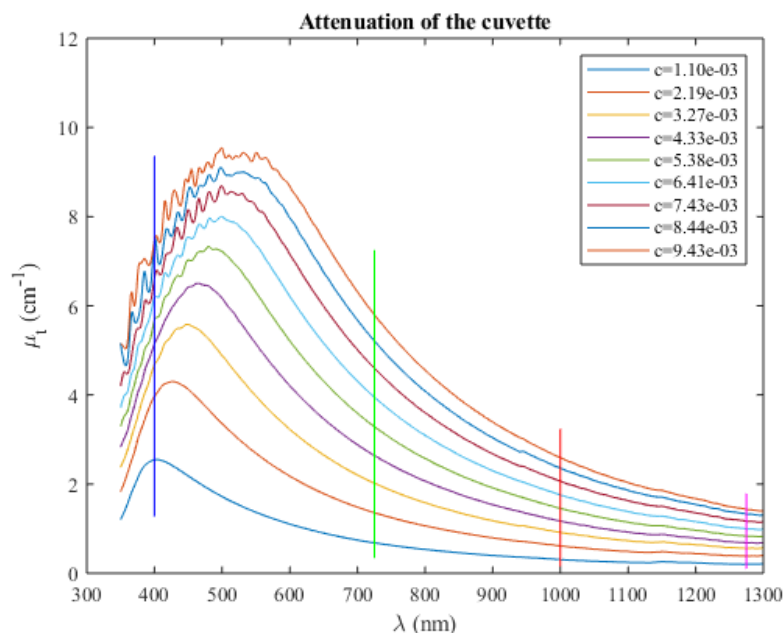
Figure 4.8 Attenuation coefficient in the cuvette for different wavelength and different intralipid concentrations.

The average attenuation is shown in figure 4.10. This result fits nicely in the plot from reference [19]. That literature study combines multiple researches and plots the graphs altogether. Our measurement has been included in the original figure published in the paper. The result fits nicely in the plot and can be seen in figure 4.11. Since the literature did not measure below a wavelength of 500 nm, it would be interesting to know if the decrease in the curve below 550 nm is valid. To do this, the measured values were compared with a simulation made with the Mie scattering calculator of Philip Laven (http://www.philiplaven.com/mieplot.htm). The simulation assumed perfectly spherical particles with 300 nm diameter and refractive index shown in table 4.1. The particle diameter was chosen as an average of the Particle Size Distribution (PSD) of [20]. The refractive indices were taken from [21]. The result is plotted in figure 4.10 as well. It is important to note that the simulation gives the extinction cross section, which has a linear relation with the attenuation.
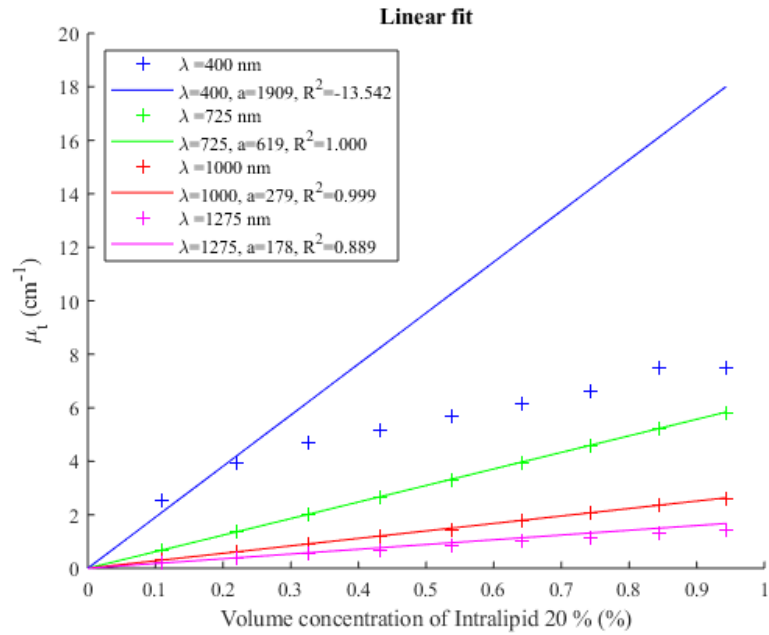
Figure 4.9 Attenuation coefficient of the cuvette mix compared to the concentration of Intralipid, for various wavelengths.
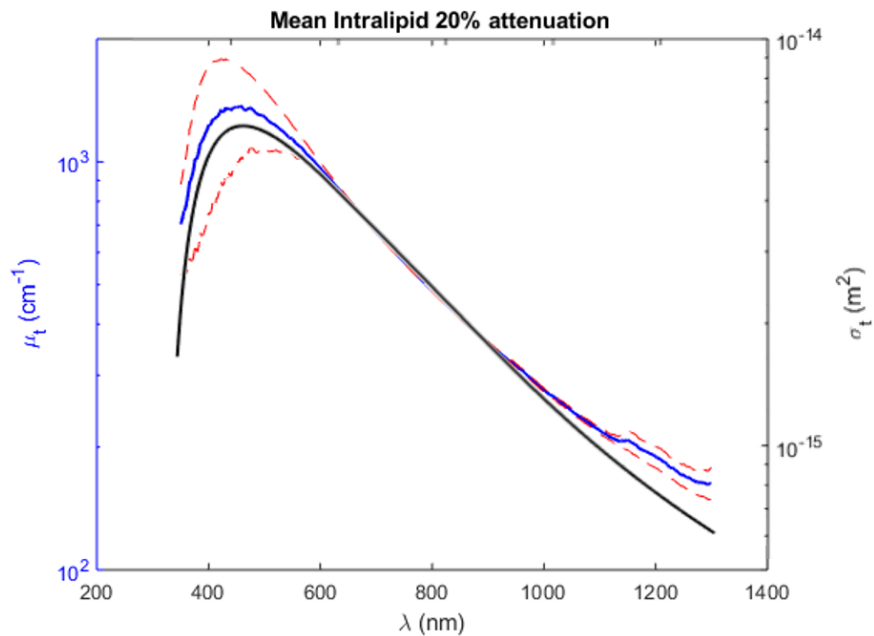

Figure 4.10 Simulated shape for the attenuation coefficient of droplets with diameter and refractive index of table 4.1.
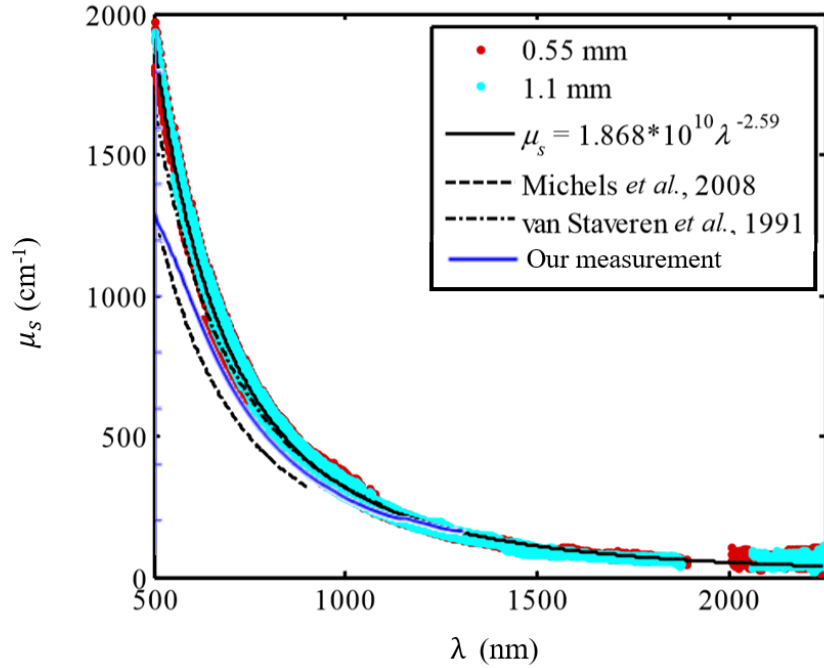
Figure 4.11 Attenuation coefficient of the cuvette mix compared to the concentration of Intralipid, for various wavelengths.

Table 4.1 Refractive index used in the simulated Mie plot.

λ (nm)	400	600	800	1000
n	1.366	1.362	1.358	1.354

The correlation is rather high considering the simplifications that had to be made, which increases the legitimacy of the measurement. Reference [15] also mentions that the scattering coefficient for intralipid is much higher than its absorption coefficient. In order to facilitate the making of the tissue mimicking samples in section 5.1.2 we will make the assumption that intralipid is a purely scattering medium, or in other words that $\mu_s = \mu_t$.

In this chapter we have thus found values for μ_a of ink and μ_s of intralipid for various wavelengths. Thanks to this information, tissue mimicking phantoms can know be created with known attenuation. The next chapter will therefore explore the making of these phantoms, as well as the time-of-flight and the simulation procedure used in this work.

Chapter 5

Photon time-of-flight: Experimental and MC simulation setup

Photon Time-of-Flight Spectroscopy (PTOFS) is a method that analyses the time response of a light pulse in a studied sample. This is done by sending a monochromatic light pulse of a few hundredths of a nanosecond through a medium and measuring the time it takes for a photon to arrive at the detector. This time depends on the speed of light in the medium and the distance the photon has traveled in the medium. If the sample is homogeneous, it can be safely deduced that the speed of light is on average constant. Hence the path length becomes the important factor. The average path length depends on both the scattering and absorption coefficient. When a material has a higher scattering coefficient, light spreads more in the sample, which results on average in a longer path in the sample and thus a longer path length. A medium with high absorption finds most of the photons with a long path absorbed. Only photons with short travelling distance survive, which gives rise to a small path length. Based on the fact that every photon takes another path, with another path length, the whole shape of the pulse depends on μ_a and μ_s. The way both coefficients affect the signal is however not the same. Therefore it is mathematically possible to differentiate them and find the initial values thanks to an algorithm. It is also interesting to note that the whole PTOFS procedure that is detailed in this chapter can be applied either to transmitted or to reflected light. It was decided to work in reflection because the scattering coefficient was high, which means that most of the intensity scattered back on the input surface.

5.1 Experiment

5.1.1 Setup and method

The time-of-flight setup that is used in Lund was build by A.A. Subash and is explained in details in [22]. The schematic of the whole setup is shown in figure 5.1.
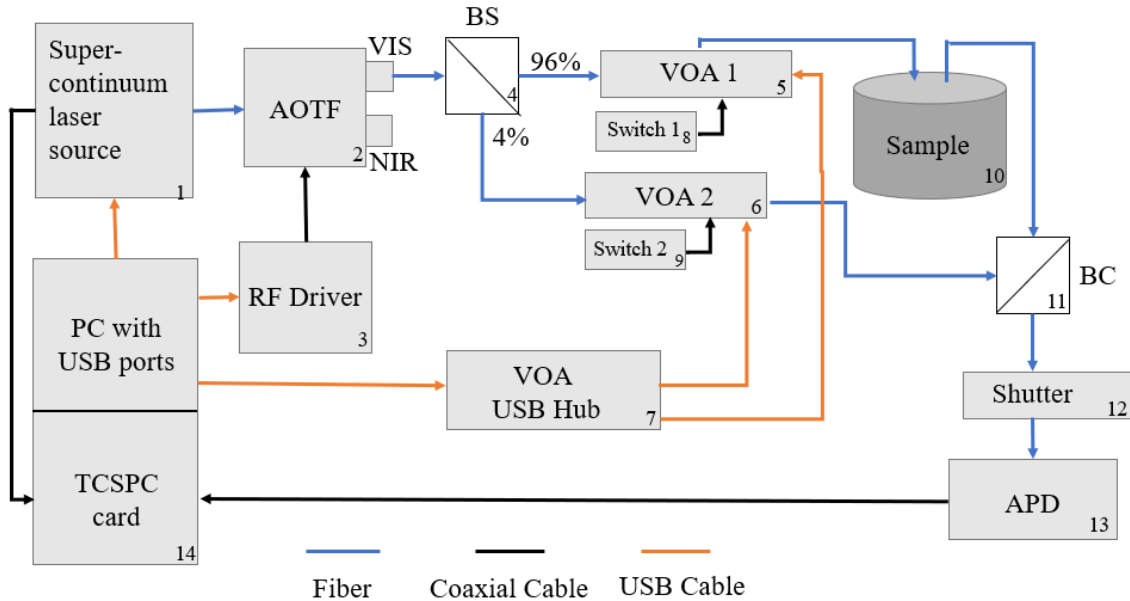

Figure 5.1 Schematic of the setup used for PTOFS.

A Photonic Crystal Fiber (PCF) super continuum source (Model SC480-10 , FianiumLtd, Southampton, UK) (1) was used to provide pulsed laser light in a wavelength range going from 480 nm to 2400 nm. It generates pulses with a Full Width at Half Maximum (FWHM) less than 100 ps with a repetition rate of 80 MHz. The obtained pulse was filtered with an Acousto-Optic Tunable Filter (AOTF) (Model AOTF-DUAL with crystals VIS, NIR1 or NIR2, Fianium Ltd, Southampton, UK) (2) in order to obtain a suitable wavelength. The AOTF has two different crystals inside, suited for different wavelength regions, and two different outputs, one for each crystal. The two spectral regions are from 500 nm to 700 nm for the Visible (VIS) output and 650 nm to 1000 nm for Near InfraRed (NIR). The AOTF was controlled via the computer through a Radio Frequency (RF) driver (3). The light pulse then went through a gradient index multi-mode fiber (400 μm/640 μm core/cladding diameter, Leoni Fiber Optics, Germany). The beam was then split in two via a beam splitter (4). One of the pulses goes to the sample and has most (96%) of the energy. This pulse was used to do the measurement. The other pulse had 4% of the energy and served as reference signal for the time cycle. Both pulses went trough an Variable Optical Attenuator (VOA) (OZ

OpticsLtd, Ottawa, Canada) (5,6). The VOA were individually controlled via the computer and cover a range from -40 dB to -3 dB. The signal beam then went to the sample and was delivered via a needle. The needle was put in contact with the surface of the liquid. Part of the resulting light was then collected via another needle in contact with the same surface. A visual representation of the sample and the needles is shown is figure 5.2. This second needle was at an adaptable distance L from the first needle that ranges from 0.75 cm to 5cm. The result was amplified in an Avalanche Photo-Diode (APD) (PD1CTC Micro Photon Devices, Bolzano, Italy) (11). The photo-diode is protected by a shutter (OZ Optics Ltd, Ottawa, Canada) (10). The reference beam goes the same shutter and APD thanks to a beam combiner (9). The amplified signal from the APD terminates in a Time Correlated Single Photon Counter (TC-SPC). The TC-SPC is mounted to a PC card (Model SPC-130 or SPC-130EM, Becker & Hickl, Berlin, Germany) (12).
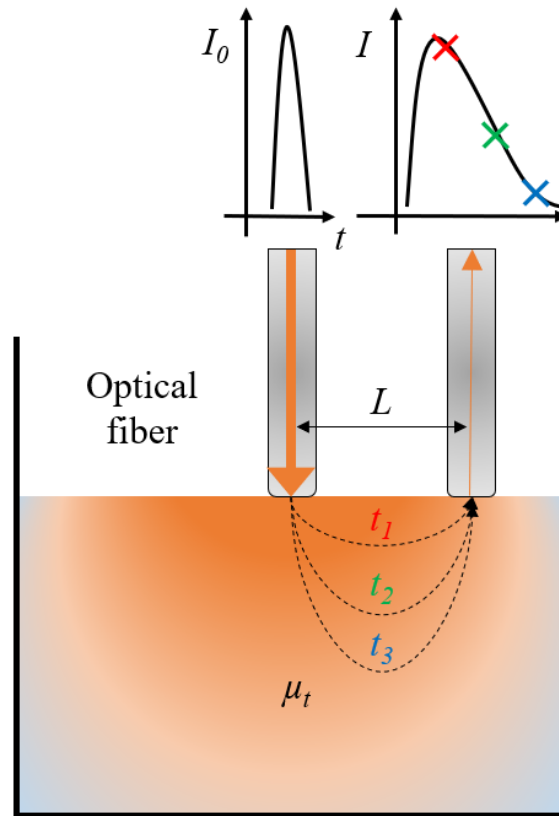

Figure 5.2 Representation of the needle-sample alignment used for PTOFS as well as the time broadening of the input pulse with intensity I_0. In the figure $t_1 < t_2 < t_3$ and represent the time a photon taken to walk shown path.

To achieve a full time of flight measurement, the following train of thought is followed. The laser sends out a short broadband pulse (480 nm to 2400 nm). The AOTF selects a

wavelength window to filter out according to the experimenter. One part of the signal goes to the sample and is detected with the APD and TCSPC. By tuning the two attenuators, it is possible to make sure that only one photon gets amplified every cycle and arrives at the detector. This starts a Constant Fraction Discrimination (CRD) time counting process. This time counting process is ended by the expected reference pulse of the next cycle and the time-of-flight is put into a histogram with 3.05 ps binsize. This process is repeated for a large number of pulses to have a significant histogram.

5.1.2 Measurement parameters

This section sets the input parameters for the experimental measurements. The different cases that were analysed are:

- Water-intralipid mixtures at 1 cm fiber separation.

- Water-intralipid mixtures at 2 cm fiber separation.

- Water-ink-intralipid mixtures at 1 cm fiber separation.

These three cases were decided in order to analyse how well the simulation tool handles scattering, absorption and different distances. No water-ink mixtures has been made since ink does not reflect the input signal. First, a wavelength for laser-light has to be chosen. 600 nm was chosen since the absorption and scattering coefficient is one of the highest we know with small error bars. The high coefficient has the practical benefit of using less fluid in order to achieve a desired $/mu_a$ and μ_s We can now start by preparing the water-intralipid mixtures and assume the absorption coefficient to be zero. When doing so, the scattering coefficient can rightfully be challenged. Afterwards, when the reliability for scattering parameter of the simulation tool is known, the ink was added to analyse the absorption parameter.

In these series of measurement 5 series of samples were created. They consisted of 250 ml of de-ionized water mixed with a pippeted volume of intralipid. This volume as well as the desired μ_s at 600 nm is transcribed in table 5.1a. Each of these samples has been measured with a fiber separation L of 1 cm and 2 cm. Every measurement series has been made and measured at least twice to minimize systematic errors. When calculating μ_s in the table, the total volume of liquid is approximated to be a constant value of 250 ml. In each measurement series, μ_s of a very diluted solution (0.150 ml and 0.450 ml) was measured. This was to make sure that the pipette work was done correctly and to analyse if the different batches of intralipid or the aging of intralipid give different results. In the ink-intralipid series 8 samples were created for each 3 different ink concentration. In order to do so, 250 ml of ionized water was mixed with a pippeted volume of ink and intralipid. The volume of

intralipid as well as the desired μ_s and μ_t is showed in table 5.1b for $\mu_a = 0.5$ cm^{-1}, in table 5.1c for $\mu_a = 1$ cm^{-1} and in table 5.1d for $\mu_a = 1.5$ cm^{-1}. The total volume in all tables is approximated to be constant at 250 ml. Each sample has been measured at a fixed fiber distance $L = 1$ cm. A reference measurement was also conducted for two reasons. The first reason is to analyse the time stretch of the reference time pulse with the measured pulse. The second reason is to have a precise input parameter for the MC tool. In that measurement, the signal pulse follows the same path as before, except that the fibers were positioned in on both sides of a sheet of black paper.

Table 5.1 Matrix representing the intralipid and ink composition of measured sample as well as the desired μ_s, μ_a and μ_t for that measurement.

(a) Solutions of only intralipids for $L = 1$ cm and $L = 2$ cm.

Intralipid (ml)	0.9	1.5	3.75	6.0	8.25	10.5	12.75	15
μ_s (cm^{-1})	3.6	6.0	15	24	33	42	51	60
μ_t (cm^{-1})	3.6	6.0	15	24	33	42	51	60

(b) Solutions of intralipids and ink for $L = 1$ cm and $V = 1.4$ ml giving $\mu_a = 0.5$ cm^{-1}.

Intralipid (ml)	0.9	1.5	3.75	6	8.25	10.5
μ_s (cm^{-1})	3.6	6.0	15	24	33	42
μ_t (cm^{-1})	4.1	6.5	15.5	24.5	33.5	42.5

(c) Solutions of intralipids and ink for $L = 1$ cm and $V = 2.8$ ml giving $\mu_a = 1$ cm^{-1}.

Intralipid (ml)	0.9	1.5	3.75	6	8.25	10.5
μ_s (cm^{-1})	3.6	6.0	15	24	33	42
μ_t (cm^{-1})	4.6	7.0	16	25	34	43

(d) Solutions of intralipids and ink for $L = 1$ cm and $V = 4.2$ ml giving $\mu_a = 1.5$ cm^{-1}.

Intralipid (ml)	0.9	1.5	3.75	6	8.25	10.5
μ_s (cm^{-1})	3.6	6.0	15	24	33	42
μ_t (cm^{-1})	5.1	7.5	16.5	25.5	34.5	43.5

Some of the recorded IRF are in shown in 5.3. As can be seen from the figure, the shape of the pulse varied very little. Therefore one reference pulse can be used in the simulation tool, which is simply the average of all measurements.

5.2   Simulation

All the input parameters for the simulation tool are detailed and discussed here. First, the dimension of the voxel had to be decided. In order to include most of the backscattering, and still keep the simulation time reasonable, the voxel size was chosen to be 5 times the fiber distance. Afterwards, the scattering coefficient had to be set. This is done in the program by setting the optical depth. Since the voxel size is known, τ can be found easily. Then the refractive index of water and of the scattering particles was set. $n_r = 1.331$ was used for water and $n_p = 1.36$ were used for the particles [21]. Then, the fiber distance had to be set. This is done by putting a mask on the receiving face(s). In our case, the same face as the input signal since we measure reflection. The mask is circular in order to measure all the signal at distance L from the input fiber. Afterwards, the laser parameters were set. The wavelength of the laser was put at a sharp 600 nm. The input pulse was put by taking the average of several IRFs taken with PTOFS. The results is shown in 5.3. The laser beam entered in the center of one side of the cube, perpendicular to that side.
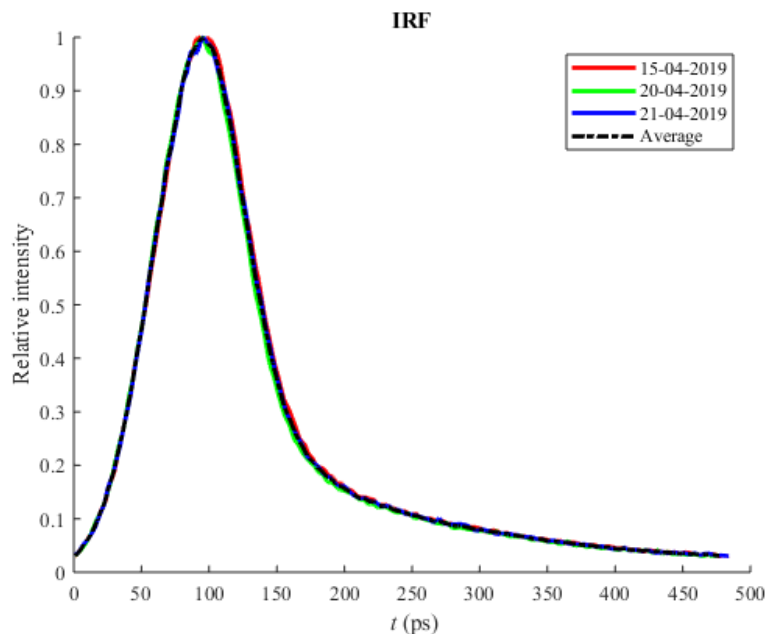

Figure 5.3 Some measured IRF with corresponding day of recording. The average of the IRFs used in the simulation tool, in black.

The scattering phase function was calculated from a particle size distribution. One of the distribution that was chosen is the one that Michel proposes in [23], based on the work of Van Staveren [24]. This particle size distribution has empirical formula $N(d) = 10^{-4.151d}$, for d between 25 nm and 473.9 nm. The corresponding PSD, as well as its corresponding phase function is shown in figure 5.5a. Another PSD, based on the recent work of Raju [20], is shown in figure 5.5b, along with the corresponding scattering phase function. The distribution shows strong agreements with the one measured in Wen [25].
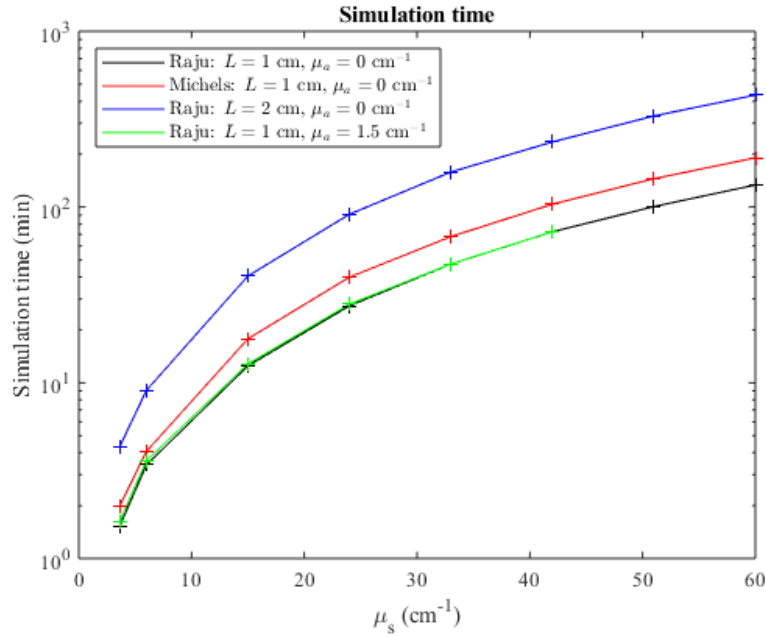
Figure 5.4 Computation time for some of the simulations performed in chapter 6.

When all the parameters are initialized, a simulation can be performed. 10 billion photons were sent in every simulation to be able to compare the intensities between simulations and still have a good SNR in the weakest case. Some examples for the simulation time are shown in figure 5.4. Two examples of the final result of the Monte Carlo are also given in figure 5.6.

In this chapter we have explained and initialize the measurement and simulation procedure. In the next chapter, the results of both measurement and simulation is compared and discussed.
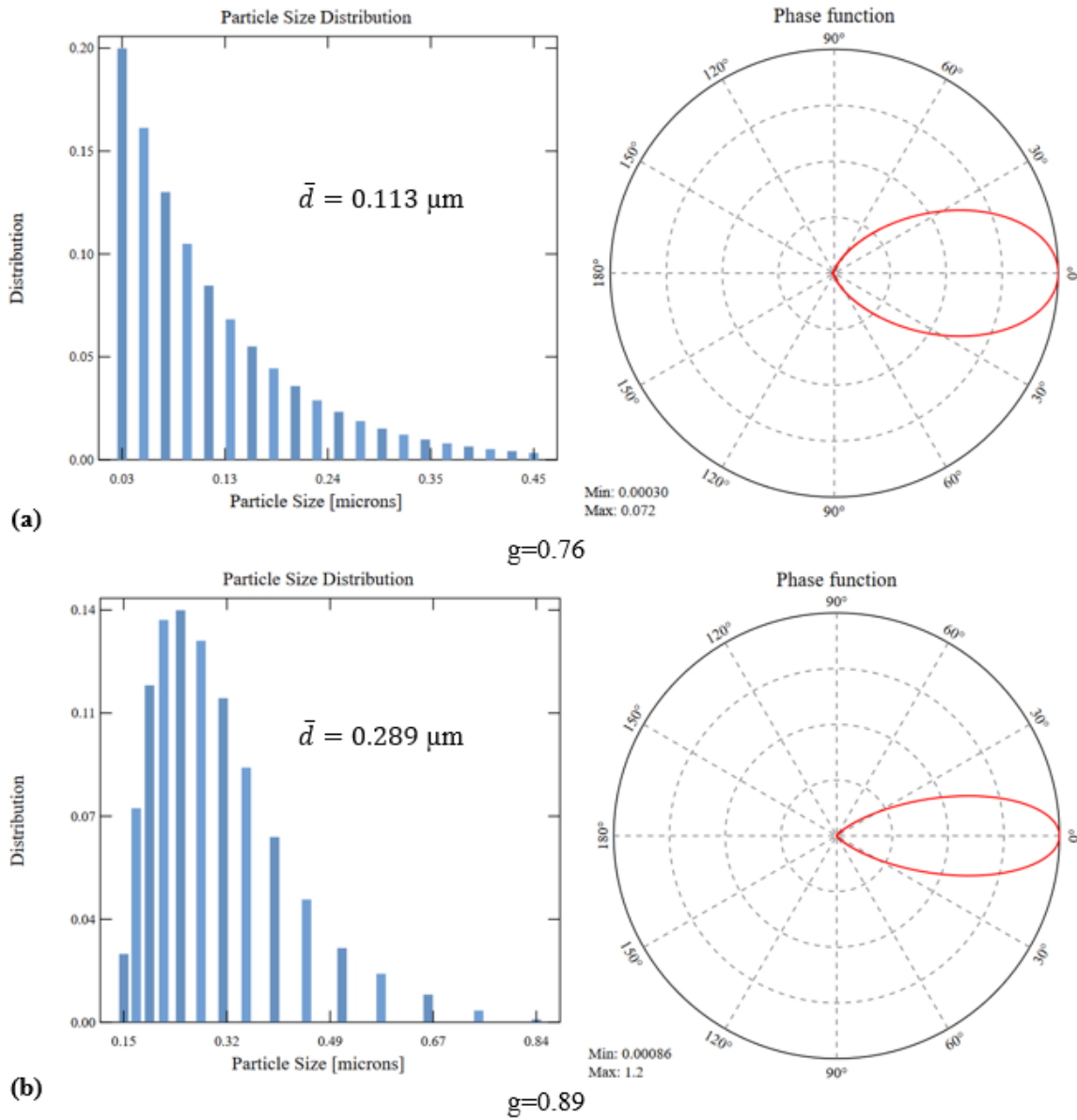
Figure 5.5 Image of the two particle size distribution used in this work. The PSD is given on the left and the corresponding phase function on the right. The images were taken with https://multi-scattering.com/. **(a)** The PSD found in Michels [23]. **(a)** The PSD found in Raju [23].

(a)

(b)
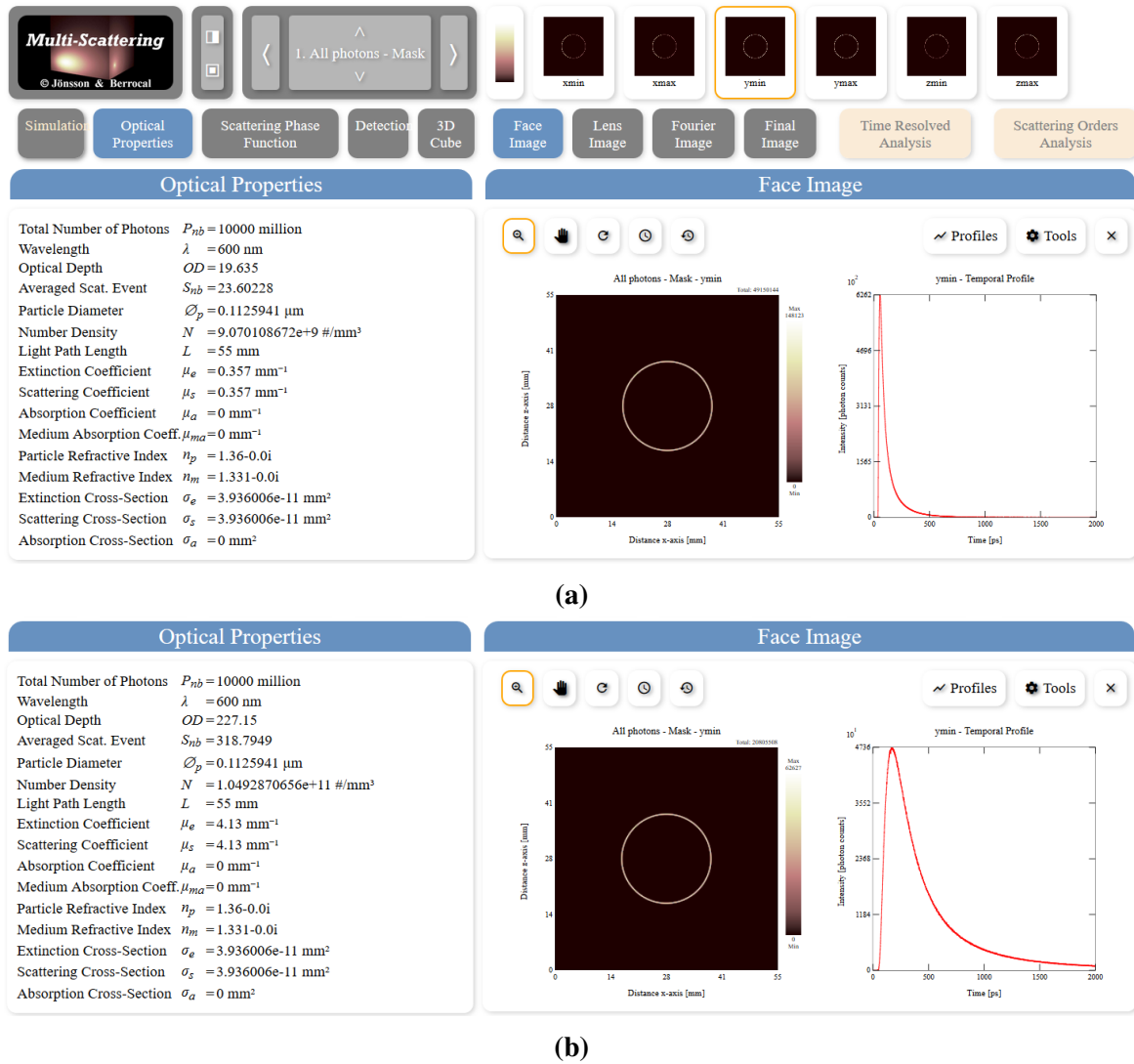
Figure 5.6 Examples of input parameter of the Monte Carlo, taken from https://multi-scattering.com/. In **(a)**, $\mu_s = 0.357$ (cm^{-1}) and in **(b)** $\mu_s = 4.13$ (cm^{-1}). The increase of the temporal response in **(b)** can clearly be seen.

Chapter 6

Results comparison and discussion

The results are split in three parts. In the first part, the relative intensity of the measured time signal is plotted along the simulations in order to analyse the pulse shape. The first analysed case is when the absorption is 0 and the fiber separation is 1 cm. The result of the measurements and simulations can be found in figure 6.1. In each of the sub-figures, the IRF precedes the measured and simulated pulse. The measured pulse is the time stretch of the IRF after interacting with the sample, measured with PTOFS. The Michel simulated pulse is the output of the simulation tool after using the Michel PSD and the input parameters discussed in the previous chapter. The Raju simulated pulse is the output of the simulation tool after using the Raju PSD and the and input parameters discussed in the previous chapter. The appropriated FWHM plot is shown in figure 6.6.a. From the figures, numerous pulse behaviors can be mentioned.

- The measured and simulated pulse are broader than the input pulse.

- The measured and the simulated pulses time stretch more for higher μ_s. This is because the average number of scattering interactions of a photon increases with μ_s. This means that its average path length increases and therefore the time-of-flight.

- The shape of all the pulses are similar and consistent.

- For small μ_s, the FWHM of the Michel pulse is smaller than the measured value, then gets almost equal to it at $\mu_s = 42$ cm^{-1} and is finally bigger than the measured value fort the largest μ_s. This could be an indication that the scattering phase function does not have the correct shape.

- The FWHM of the Michel pulse is smaller than the measured value and does not seem to change much relatively, when the scattering coefficient increases. This could mean

that propagating distance is not long enough. This could mean that the scattering phase function has a too small *g*.

In the second case, the absorption is 0 and the fiber separation is 2 cm. The result of the measurements and simulations are shown in figure 6.2 and the FWHM is shown in figure 6.6.b. Similar behavior can be mentioned for these pulses, except that:

- All the pulses have longer time stretch compared with the previous case. This is because increasing the fiber distance increases the number of scattering events and thus the average time-of-flight.

- The Michel pulse gets an almost perfect match when $\mu_s = 15$ cm^{-1}. Which further suggest an incorrect choice of scattering phase function.

In the third case, the absorption is 0.5 cm^{-1} and the fiber separation is 1 cm. The result of the measurements and simulations are shown in figure 6.3 and the FWHM is shown in figure 6.6.c. Similar behavior as the first case can be mentioned for these pulses, except that:

- The time stretch of all pulses is shorter than in the first case. This is because photon with long path length have a higher chance of getting absorbed. This means that they are certainly absorbed before reaching the detector.

- The FWHM of Michel are always smaller than the measured ones, and are not consistent with the ones showed in the first case.

- The FWHM of Raju are consistent with the ones showed in the first case.

In the fourth case, the absorption coefficient is 1 cm^{-1} and the fiber separation is 1 cm. The result of the measurements and simulations are shown in figure 6.4 and the FWHM is shown in figure 6.6.d. Similar behavior as the previous case can be mentioned for these pulses, except that the time stretch of all pulses is smaller.
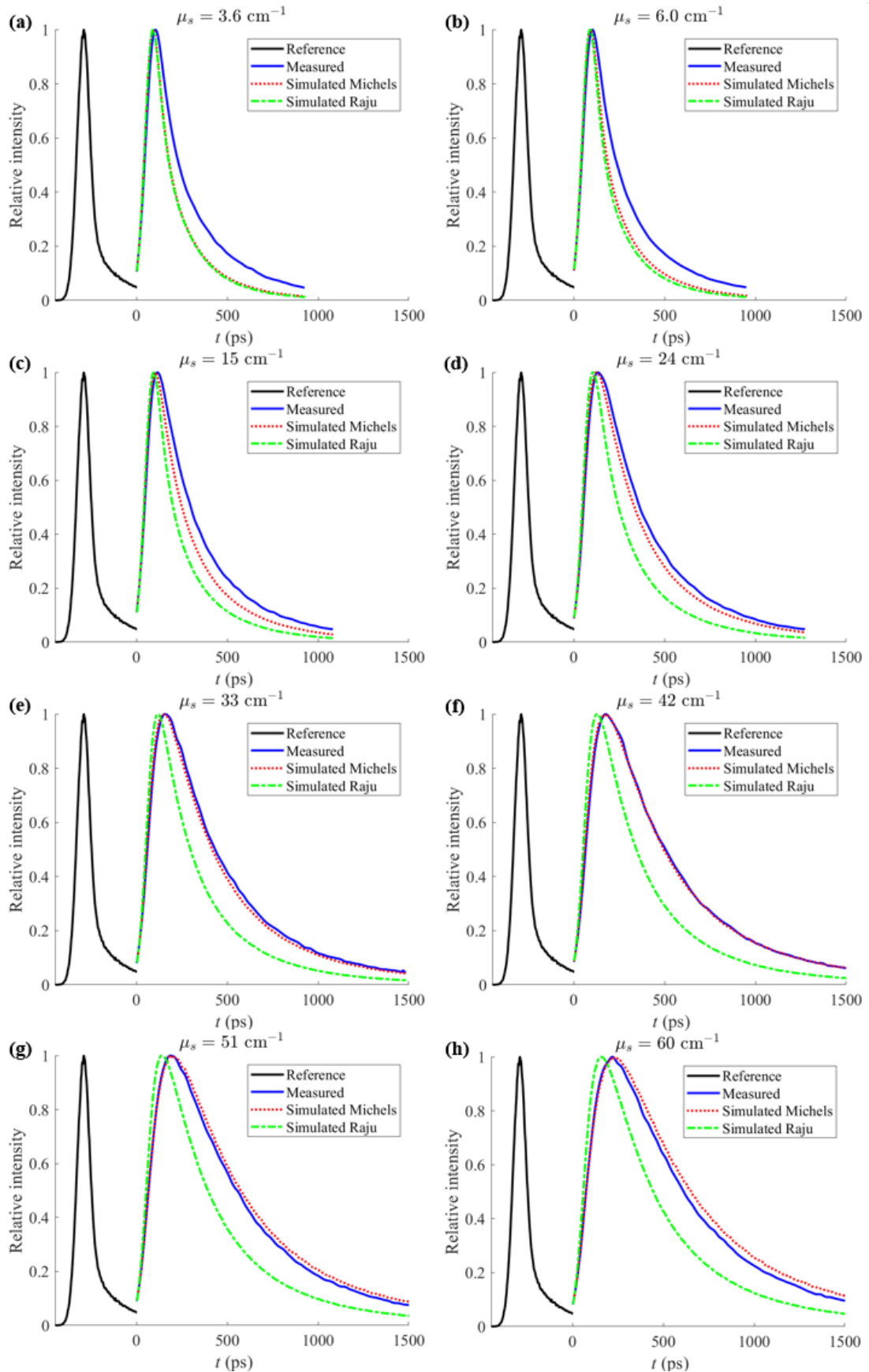
In the fifth case, the absorption coefficient is 1.5 cm^{-1} and the fiber separation is 1 cm. The result of the measurements and simulations are shown in figure 6.4 and the FWHM is shown in figure 6.6.e. Similar behavior as the previous case can be mentioned for these pulses except that the time stretch of all pulses is even smaller

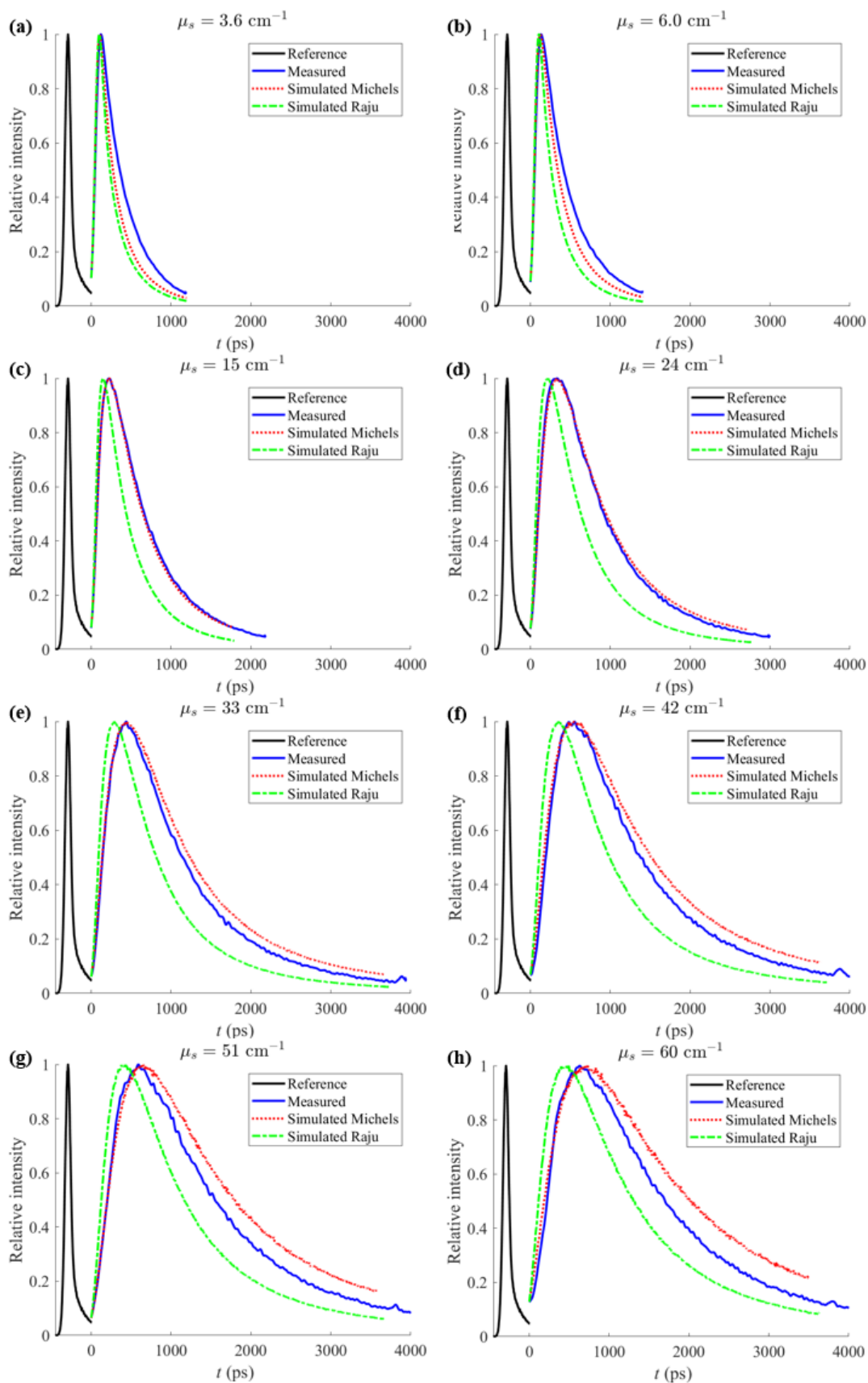**Figure 6.1** Simulated and measured results for the water-intralipid mixture at 1cm fiber separation.

Figure 6.2 Simulated and measured results for the water-intralipid mixture at 2cm fiber separation.
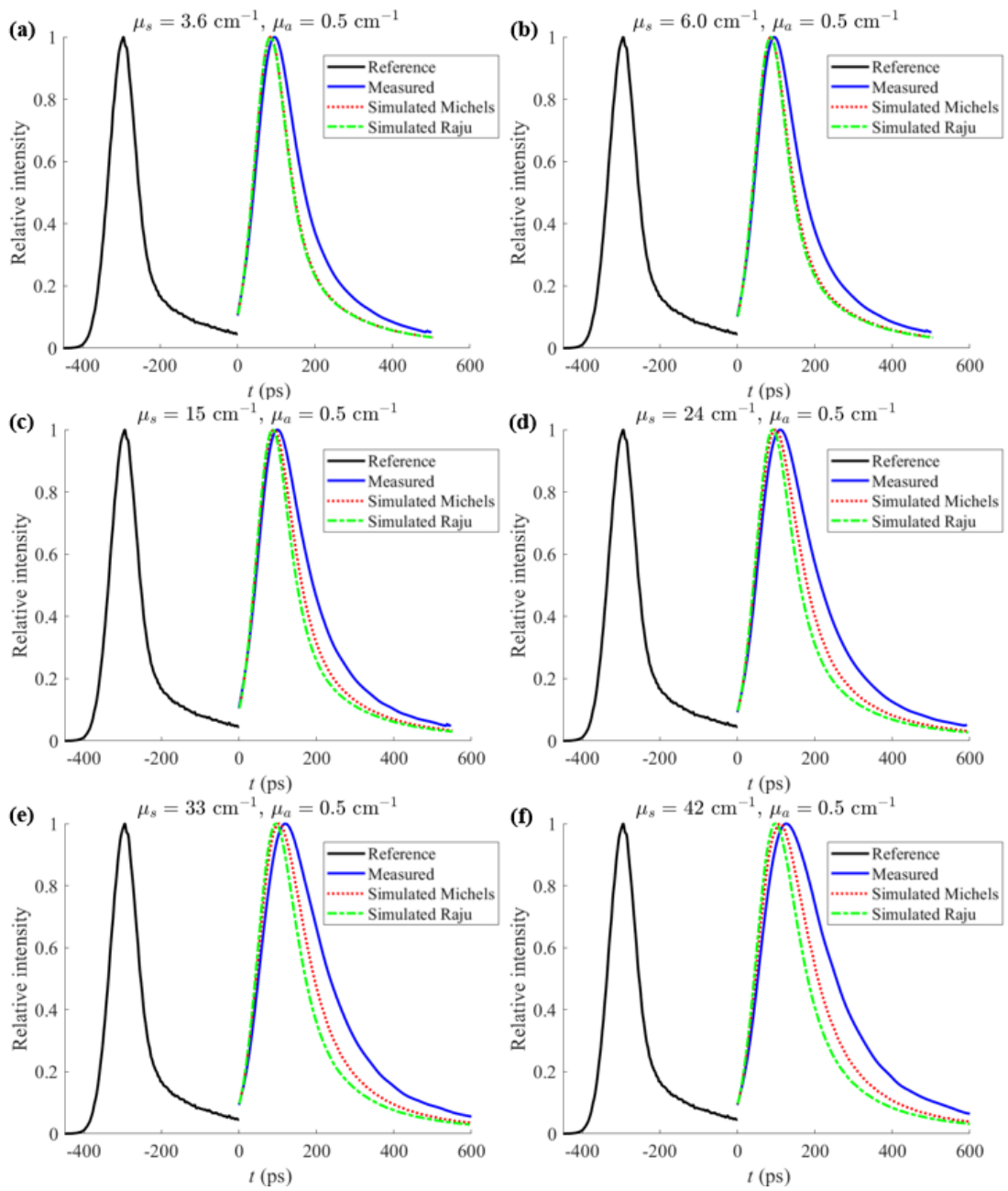
Figure 6.3 Simulated and measured results for the water-ink-intralipid mixture with 1.4 ml ink, at 1cm fiber separation.
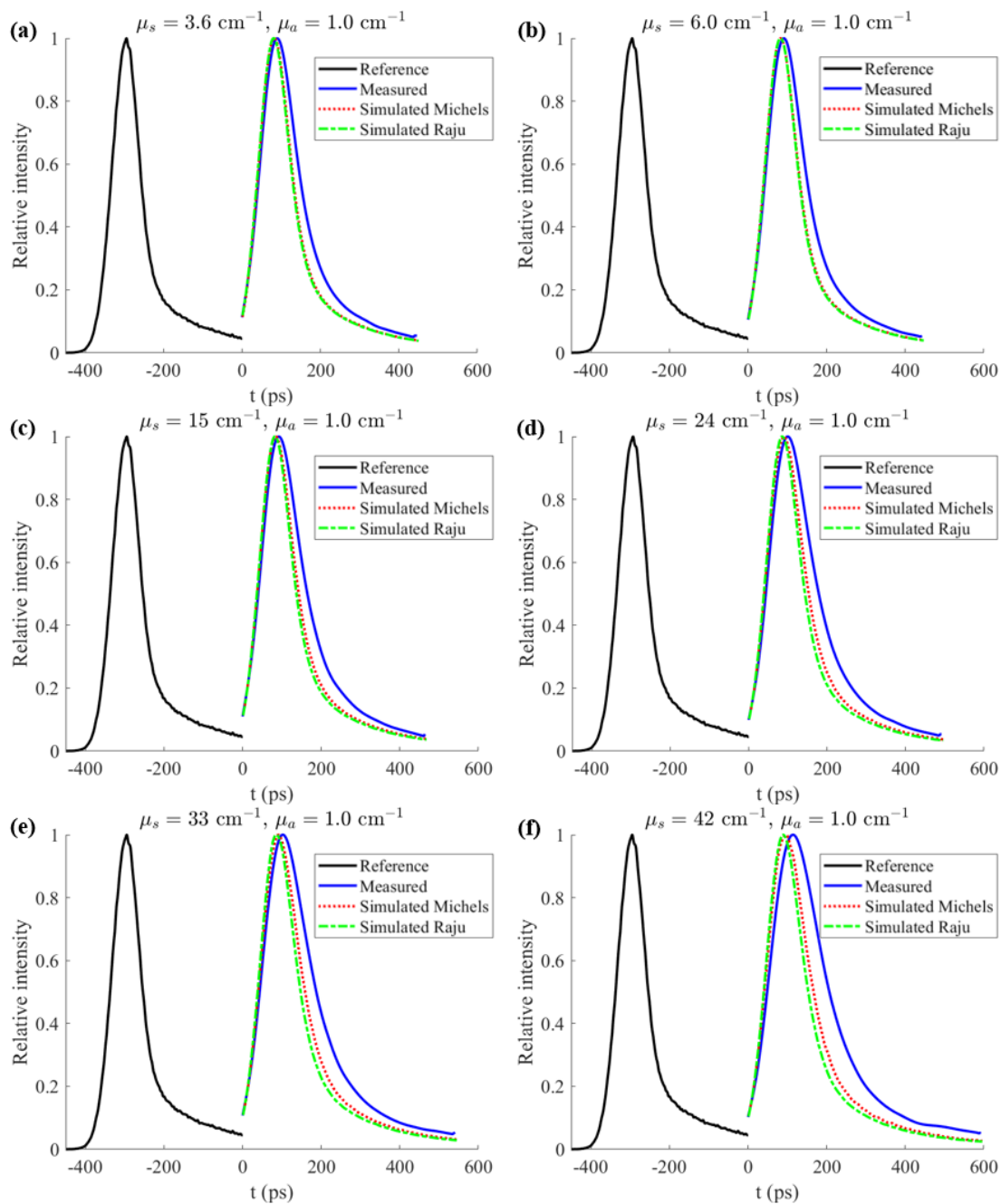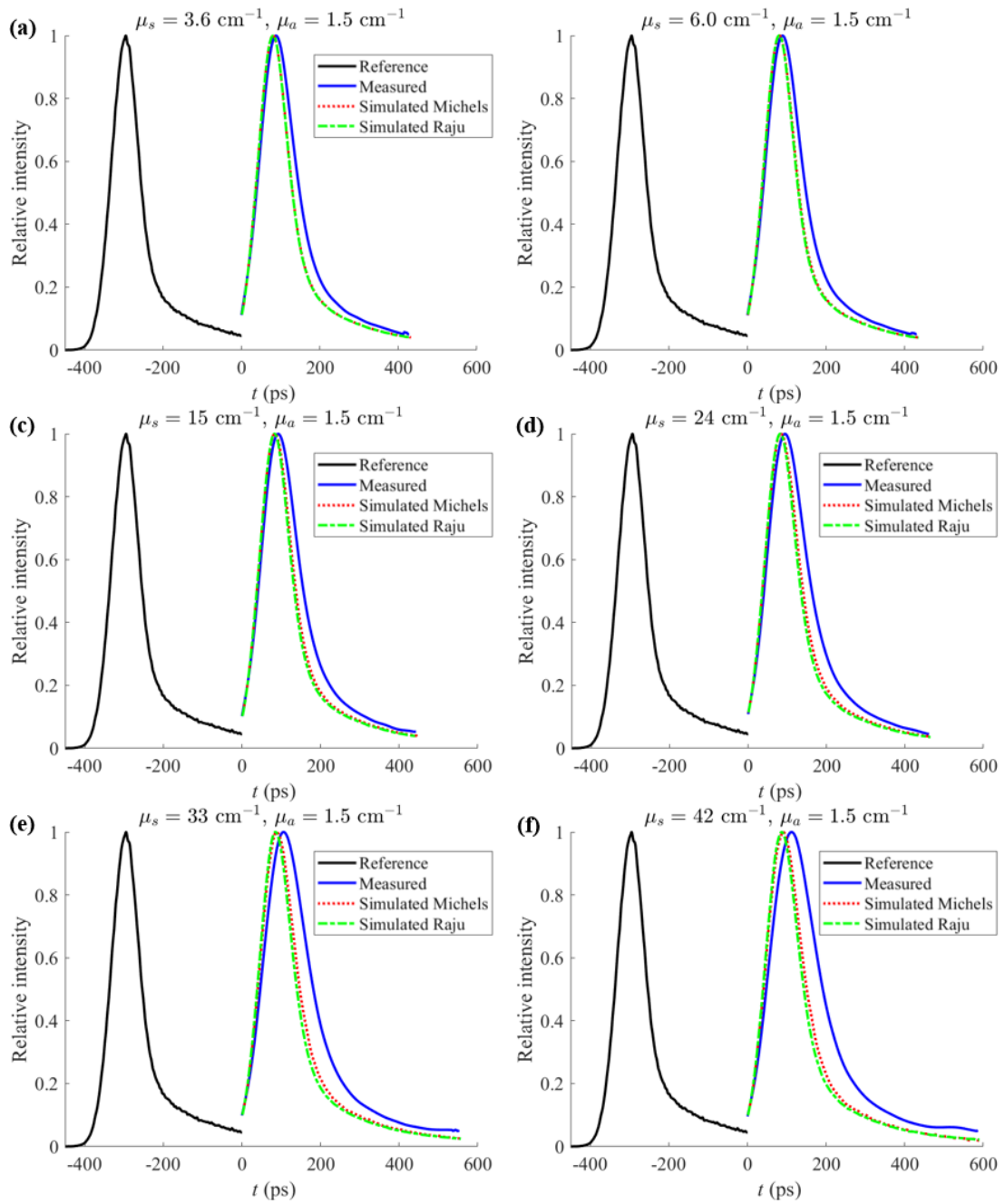
Figure 6.4 Simulated and measured results for the water-ink-intralipid mixture with 2.8 ml ink, at 1cm fiber separation.
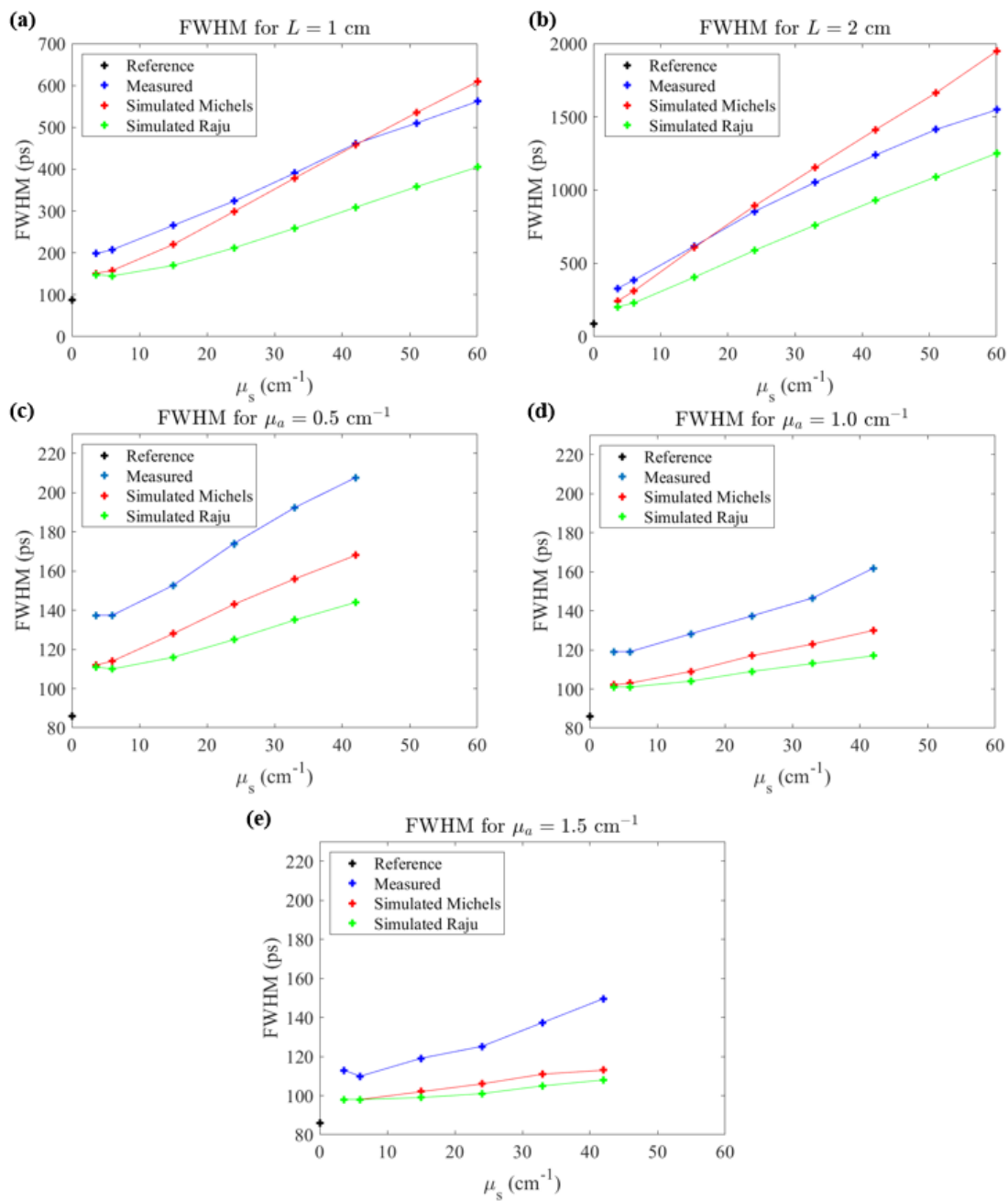
Figure 6.5 Simulated and measured results for the water-ink-intralipid mixture with 4.2 ml ink, at 1cm fiber separation.

Figure 6.6 FWHM of the pulses found in figure 6.1-6.5.

In the second part, the intensity were analysed. This was done by dividing the intensity of the pulses by the maximum intensity of the respective $\mu_s = 3.6$ pulse for measurement and simulation. The results for the first case ($L = 1$ cm and $\mu_a = 0$ cm^{-1}) are shown in figure 6.7. For the measured pulses, the attenuation induced by the attenutator has been considered in the plots. From the figures the following pulse behaviours are mentioned:

- The intensity of the pulse depends on μ_s. This can be explained by the fact that the measurement is done at a certain fiber distance and that the distance of the maximum backscattering depends on μ_s.

- For the measured case, $\mu_s = 6$ cm^{-1} and $\mu_s = 15$ cm^{-1} are the most intense pulses.

- For the Michel pulse, $\mu_s = 6$ cm^{-1} is the most intense pulse. The intensity ratio also decreases faster with increasing μ_s than in the measured case.

- For the Raju pulse, $\mu_s = 6$ cm^{-1} and $\mu_s = 15$ cm^{-1} are the most intense pulse. The intensity ratio seems to agree, except for the most intense cases were they are too high.

The results for the second case ($L = 2$ cm and $\mu_a = 0$ cm^{-1}) are shown in figure 6.8. Similar behavior as the previous case can be mentioned for these pulses, except that:

- For the measured case, $\mu_s = 3.6$ cm^{-1} and $\mu_s = 6$ cm^{-1} are the most intense pulses.

- For the Michel pulse, $\mu_s = 3.6$ cm^{-1} is the most intense pulse.

- For the Raju pulse, $\mu_s = 3.6$ cm^{-1} and $\mu_s = 6$ cm^{-1} are the most intense pulse. The results seems to agree better with the measurement.

The results for the third case ($L = 1$ cm and $\mu_a = 0.5$ cm^{-1}) are shown in figure 6.9. Similar behavior as the first case can be mentioned for these pulses, except that:

- For the measured case, $\mu_s = 6$ cm^{-1} is the most intense pulses. This is because photons with longer path lengths (higher μ_s) are more likely to be absorbed.

- For the Michel pulse, $\mu_s = 3.6$ cm^{-1} and $\mu_s = 6$ cm^{-1} are the most intense pulse.

- For the Raju pulse, $\mu_s = 6$ cm^{-1} is the most intense pulse. The results seems to agree better with the measurement.

The results for the fourth case ($L = 1$ cm and $\mu_a = 1$ cm^{-1}) are shown in figure 6.10. Similar behavior as the previous case can be mentioned for these pulses, except that for the Michel pulse, the intensities of the pulses are very low compared to the measured ones.

The results for the fifth case ($L = 1$ cm and $\mu_a = 1.5$ cm^{-1}) are shown in figure 6.11. Similar behavior as the previous case can be mentioned for these pulses.
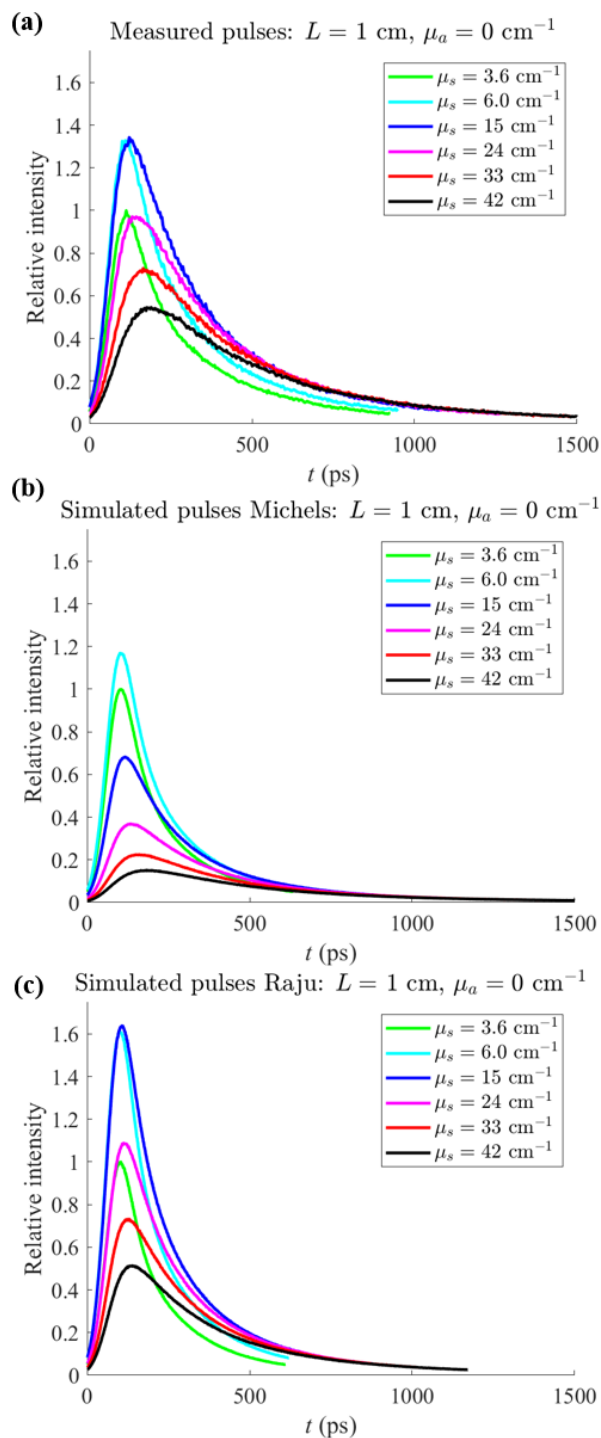
Figure 6.7 Intensity ratio of simulated and measured pulses for $L = 1$ cm and $\mu_a = 0$ cm^{-1}
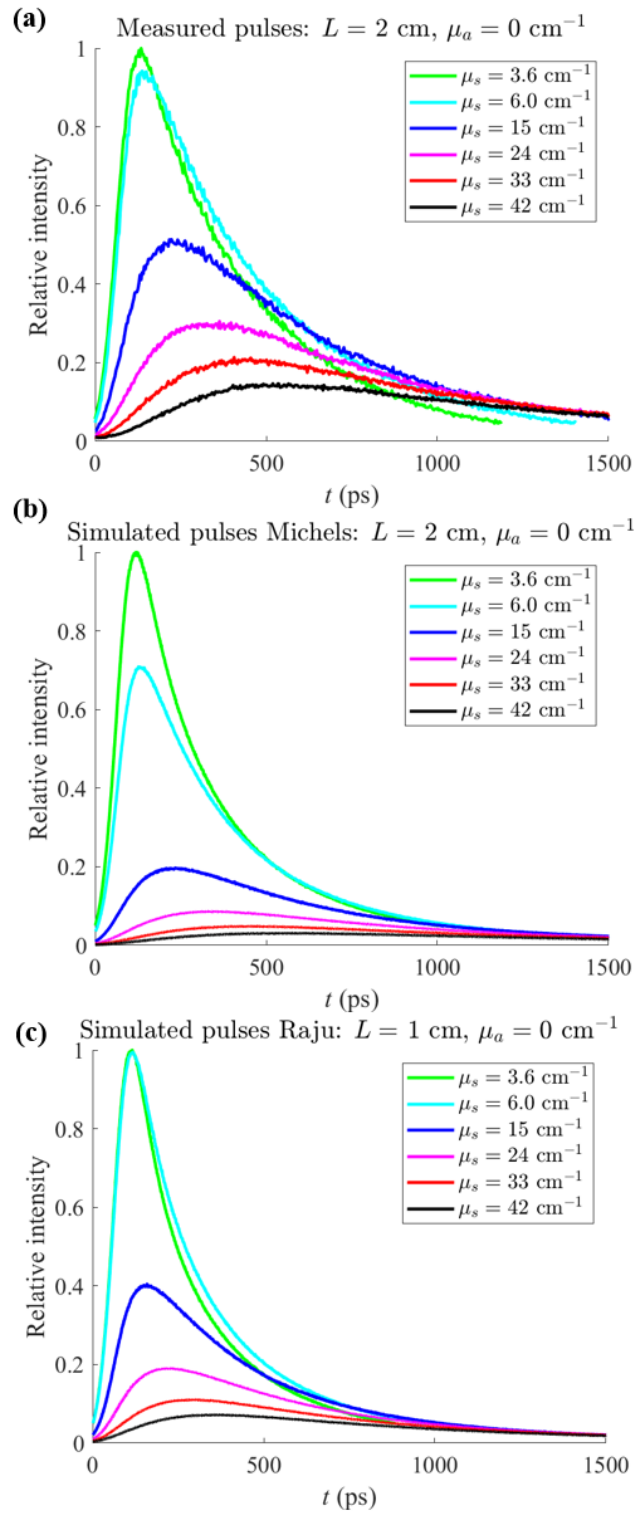
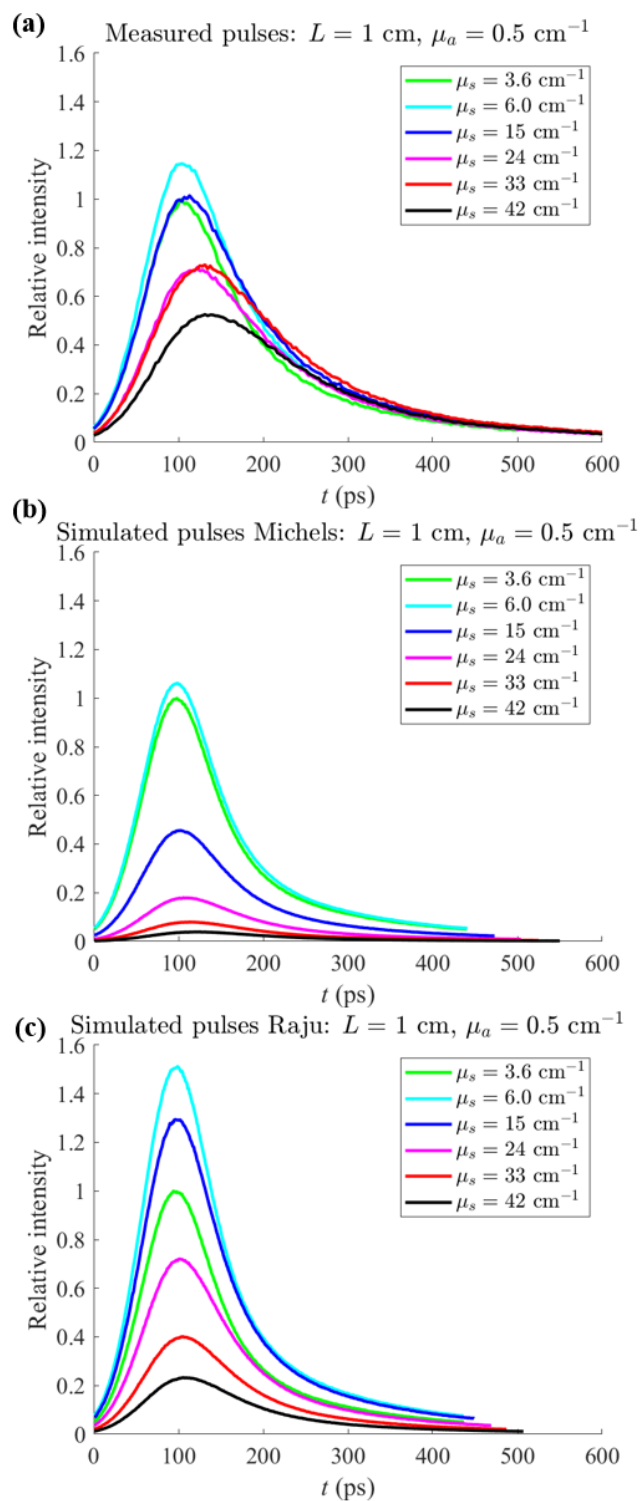**Figure 6.8** Intensity ratio of simulated and measured pulses for $L = 2$ cm and $\mu_a = 0$ cm^{-1}

Figure 6.9 Intensity ratio of simulated and measured pulses for $L = 1$ cm and $\mu_a = 0.5$ cm^{-1}

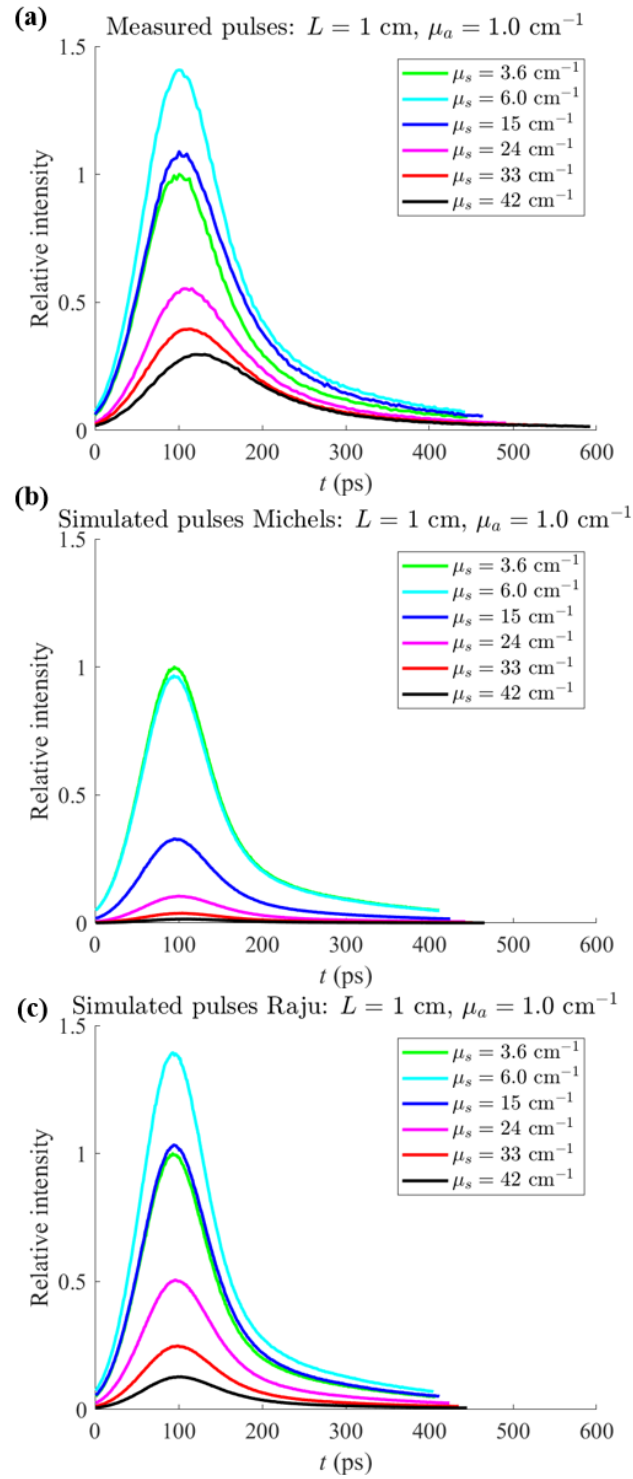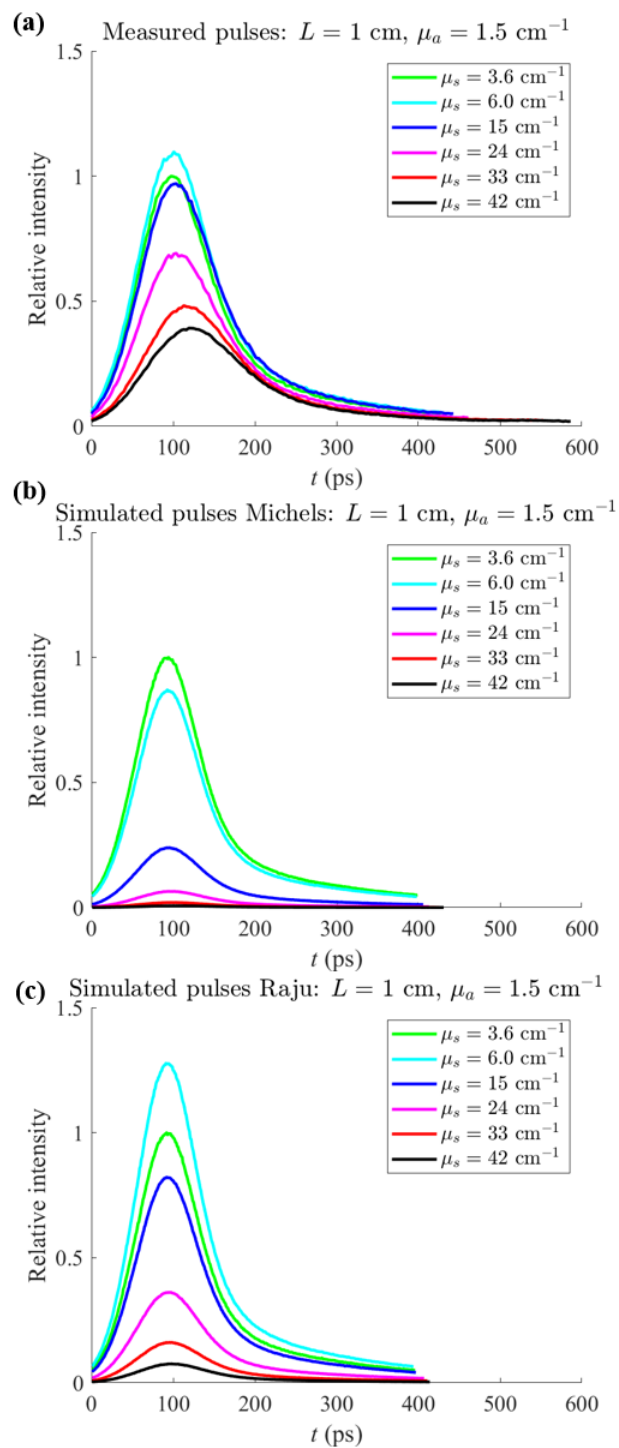**Figure 6.10** Intensity ratio of simulated and measured pulses for $L = 1$ cm and $\mu_a = 1$ cm^{-1}

Figure 6.11 Intensity ratio of simulated and measured pulses for $L = 1$ cm and $\mu_a = 1.5$ cm^{-1}

In the third part, some other input parameters were varied to study their effect. The first parameter that was analysed is the input angle of the lasers beam. Indeed, in reality light exits optical fibers with a conical angle that can be calculated with the numerical aperture. The numerical aperture of the fiber is 0.22, which means that the angle at which the light enters the medium is not $\theta_i = 0°$ but $\theta_i = \arcsin(NA/n) = \arcsin(0.22/1.33) = 9.5°$. In figure 6.12a and 6.12b the influence of the input angle is shown. This was done by comparing a simulation with acceptance angle 9.5° with the regular simulation. The results do not show any difference for these parameters.

(a)

$\mu_s = 15$ cm^{-1}

(b)

$\mu_s = 42$ cm^{-1}
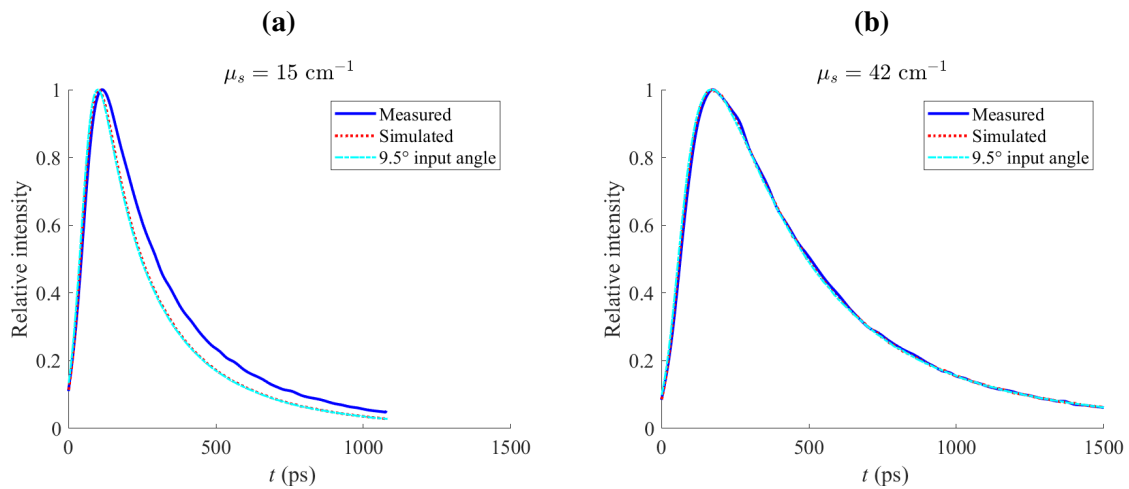
The second parameter that was analysed is the acceptance angle of the optical fiber. By default, the simulation accepts all the photons that make it to the face of the cube. To include the 9.5° calculated before, we can restrict the angle in the Fourier plane. In figure 6.13a and 6.13b, the influence of the acceptance angle is shown. The image was constructed by comparing a Fourier image that filtered out all photons with acceptance angle bigger than 9.5° with the regular simulation for that Fourier image. The results do not show any difference for these parameters.
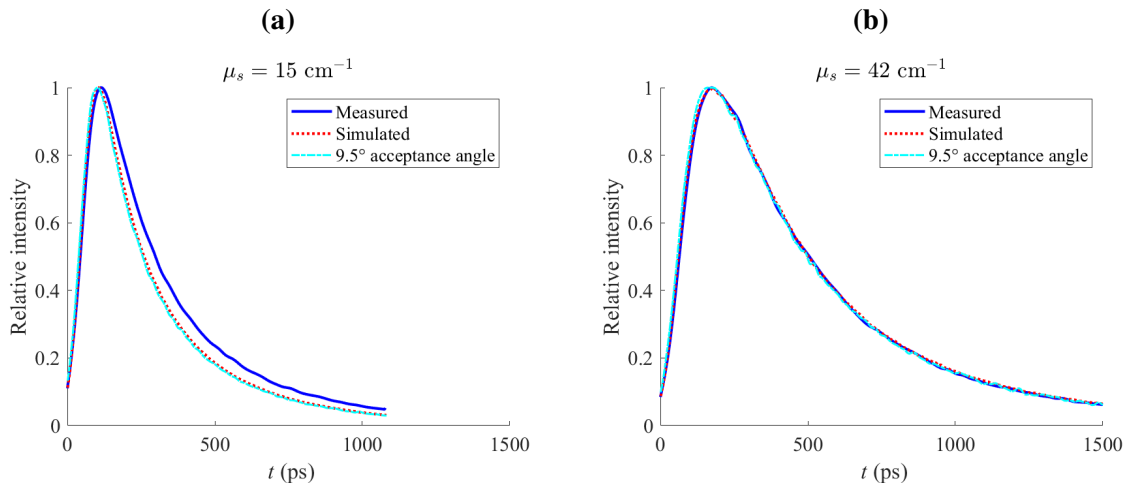
Figure 6.13 Difference when using a Fourier acceptance angle for the output fiber.

Finally, the simulation was performed for various single particle sizes in order to evaluate the impact of such variation. The different sizes used are 250 nm, 275 nm, 300 nm, 325 nm and 350 nm. The result shown in figure 6.14. It is clear from the figures that the simulations changes with particle sizes. It can also be seen that the simulation where $d = 275$ nm is closest to the measurement where $\mu_s = 15$ cm^{-1} and that the simulation where $d = 300$ nm is closest to the measurement where $\mu_s = 42$ cm^{-1}. This means that a phase function based on a single particle cannot reproduce the advanced phase function of the tissue mimicking phantom since the best match evolves with scattering coefficient. This means that a complete distribution needs to be used instead of an averaged number.
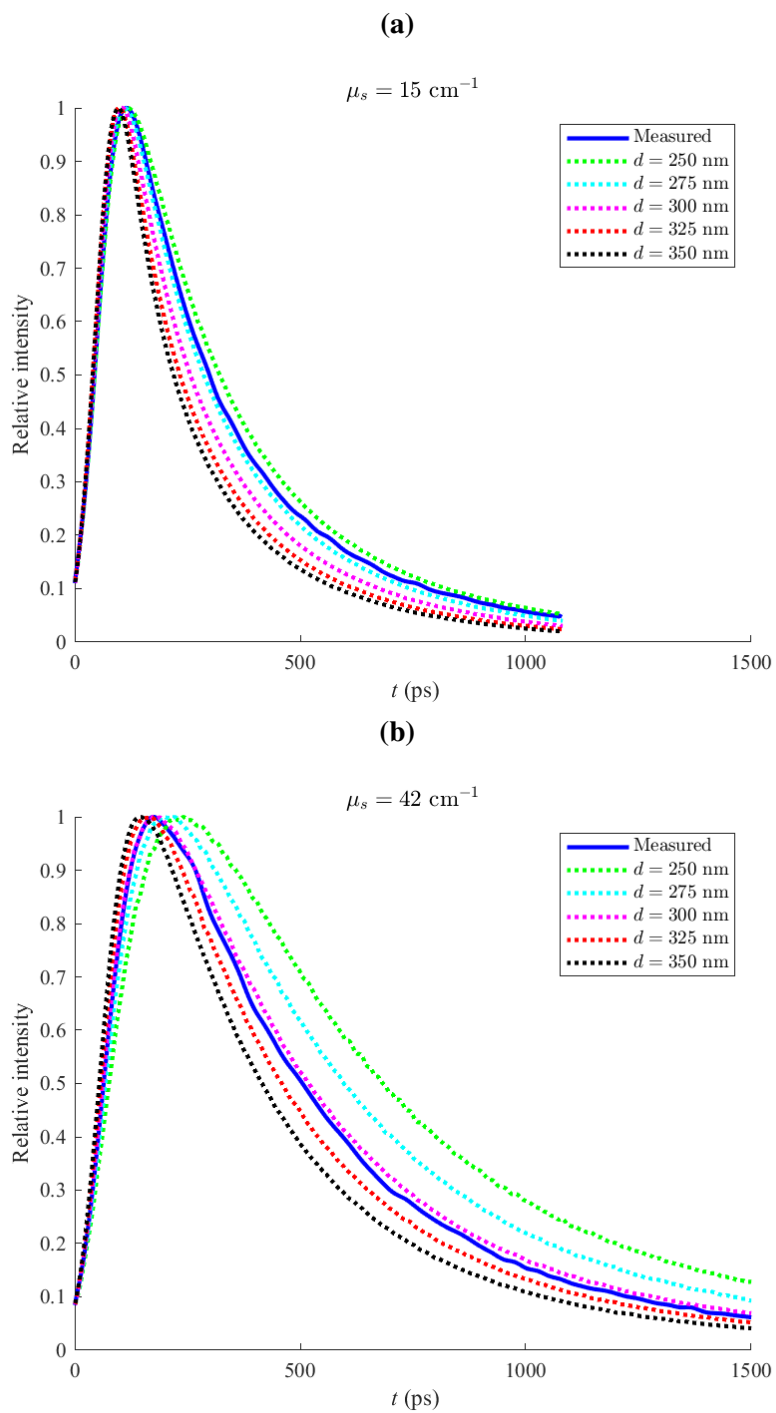
(a)

$\mu_s = 15$ cm^{-1}

(b)

$\mu_s = 42$ cm^{-1}

Figure 6.14 Difference between different particle size distributions.

Chapter 7

Conclusion and outlook

In this chapter, three main conclusion on the usage and accuracy of the simulation tool are given, as well as an outlook for further validation and improvement of the simulation software.

The first conclusion is that the simulation tool manages to reproduce measured signals rather well. Trends that are seen in the measurement are reproduced in all simulations and are best followed when the Raju scattering phase function was used. This would mean that the software can already be used for the comparison of simulated results. By this we mean that we can already analyse the relative change that a different input parameter introduces to the result. It is then highly likely that his relative change is reproduced when changing this parameter in a measurement.

The second conclusion is that the results depend on the scattering phase function. It is therefore highly recommended to have a good representation of this parameter. Using an average number for such distribution will result in erroneous simulations. Using the Henyey-Greenstein formula for the simulations will also lead to incorrect results since it cannot fully represent the scattering phase function of a distribution and is not accurate at multiple particle sizes.

The third conclusion is that since the exact particle size distribution used for the measurements in this work is not exactly know, the simulation tool cannot be entirely validated. However, the literature seems to agree that the particle size distribution of intralipid 20% is the one mentioned in reference [20], with small variation. If such is the case, the tool should still be improved in order to match the time scale found in the measurements. Nonetheless, the tool seems promising.

As an outlook for the future, several suggestions are made here. It would be interesting to measure the particle size distribution of the same intralipid particles used in the lab or measure the scattering phase function and compare these simulation with the measurement. Another

possibility is to reiterate the measurements in a medium with known particle diameter, such as micro-spheres. Micro-spheres can be purchased in various known diameters and could be used to tune the scattering coefficient replacing the intralipid. By doing so, the simulation tool will be validated in time domain for all the important input parameters. Another suggestion regards the simulation software itself. A good add on for the simulation tool would be to have the possibility to construct a structure made of multiple homogeneous cubes, but with different optical properties. This way more realistic simulations can be made on non homogeneous media and the number of applications of the tool would improve drastically.

References

[1] Qian Peng, Asta Juzeniene, Jiyao Chen, Lars O Svaasand, Trond Warloe, Karl-Erik Giercksky, and Johan Moan. Lasers in medicine. *Reports on Progress in Physics*, 71(5):056701, 2008.

[2] Ashley J Welch and Martin JC Van Gemert. *Optical-thermal response of laser-irradiated tissue*, volume 2. Springer, 2011.

[3] László Baranyai and Manuela Zude. Analysis of laser light propagation in kiwifruit using backscattering imaging and monte carlo simulation. *Computers and Electronics in Agriculture*, 69(1):33–39, 2009.

[4] Rod Frehlich. Simulation of laser propagation in a turbulent atmosphere. *Applied Optics*, 39(3):393–397, 2000.

[5] Zhi Song, Ke Dong, Xin H Hu, and Jun Q Lu. Monte carlo simulation of converging laser beams propagating in biological materials. *Applied optics*, 38(13):2944–2949, 1999.

[6] Joakim Jönsson. Acceleration and optimisation of a monte carlo code for light propagation in sprays and other scattering media. Master thesis, Lund University, 2011.

[7] Edouard Berrocal. *Multiple scattering of light in optical diagnostics of dense sprays and other complex turbid media*. Doctoral thesis, Cranfield University, 2006.

[8] Caroline Boudoux. *Fundamentals of Biomedical Optics: From Light Interaction with Atoms and Molecules to Complex Imaging Systems*. Pollux, 2016.

[9] Wai-Fung Cheong, Scott A Prahl, and Ashley J Welch. A review of the optical properties of biological tissues. *IEEE journal of quantum electronics*, 26(12):2166–2185, 1990.

[10] John H Seinfeld and Spyros N Pandis. *Atmospheric chemistry and physics: from air pollution to climate change*. John Wiley & Sons, 2016.

[11] Dominique Toublanc. Henyey–greenstein and mie phase functions in monte carlo radiative transfer computations. *Applied optics*, 35(18):3270–3274, 1996.

[12] Wolfram Hergert and Thomas Wriedt. *The Mie theory: basics and applications*, volume 169. Springer, 2012.

[13] Craig F Bohren and Donald R Huffman. *Absorption and scattering of light by small particles*. John Wiley & Sons, 2008.

[14] Joakim Jönsson and Edouard Berrocal. Simulation of light scattering and imaging of spray systems using the open-access software "multi-scattering". In *Proceedings of the 29th European Conference on Liquid Atomization and Spray Systems (ILASS-Europe 2019), Paris, France*, 2019.

[15] Paola Di Ninni, Fabrizio Martelli, and Giovanni The use of india ink in tissue-simulating phantoms. 18(26):26854–26865, 2010.

[16] L et al Determination of reference values for optical properties of liquid phantoms based on intralipid and india ink. 5(7):2037–2053, 2014.

[17] George M Hale and Marvin R Optical constants of water in the 200-nm to 200-μ m wavelength region. 12(3):555–563, 1973.

[18] W Scott Pegau, Deric Gray, and J Ronald V Zaneveld. Absorption and attenuation of visible and near-infrared light in water: dependence on temperature and salinity. *Applied optics*, 36(24):6035–6046, 1997.

[19] Ben Aernouts, Eduardo Zamora-Rojas, Robbe Van Beers, Rodrigo Watté, Ling Wang, Mizuki Tsuta, Jeroen Lammertyn, and Wouter Saeys. Supercontinuum laser based optical characterization of intralipid® phantoms in the 500-2250 nm range. *Optics express*, 21(26):32450–32467, 2013.

[20] Michael Raju and Sujatha Narayanan Unni. Concentration-dependent correlated scattering properties of intralipid 20*Applied optics*, 56(4):1157–1166, 2017.

[21] Huafeng Ding, Jun Q Lu, Kenneth M Jacobs, and Xin-Hua Hu. Determination of refractive indices of porcine skin tissues and intralipid at eight wavelengths between 325 and 1557 nm. *JOSA A*, 22(6):1151–1157, 2005.

[22] Arman Ahamed Subash. Wide-bandwidth time of flight spectroscopy of turbid media. *Lund Reports in Atomic Physics*, 2012.

[23] René Michels, Florian Foschum, and Alwin Kienle. Optical properties of fat emulsions. *Optics Express*, 16(8):5907–5925, 2008.

[24] Hugo J Van Staveren, Christian JM Moes, Jan van Marie, Scott A Prahl, and Martin JC Van Gemert. Light scattering in lntralipid-10400–1100 nm. *Applied optics*, 30(31):4507–4514, 1991.

[25] Xiang Wen, Valery V Tuchin, Qingming Luo, and Dan Zhu. Controling the scattering of intralipid by using optical clearing agents. *Physics in Medicine & Biology*, 54(22):6917, 2009.

Appendix A
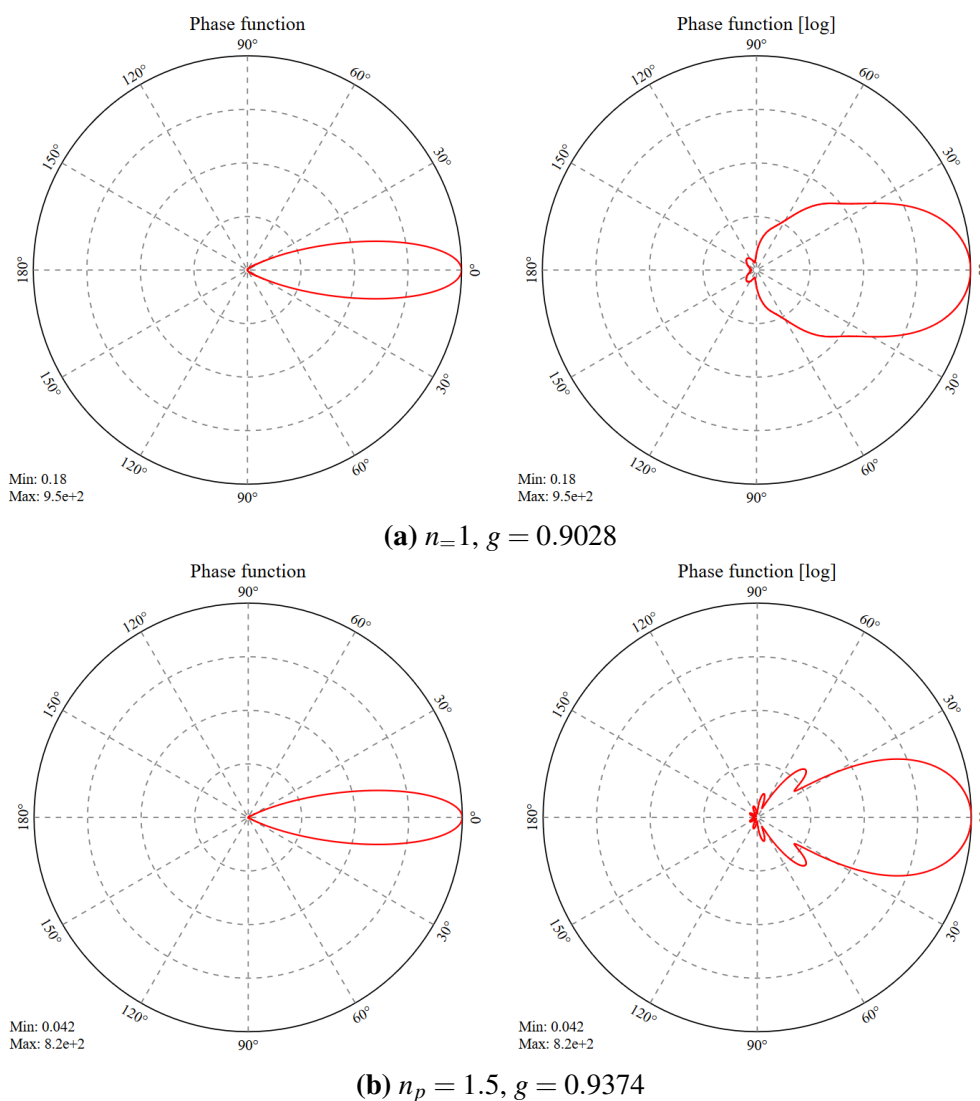
Changes in the scattering phase function

(a) $n_{=}1$, $g = 0.9028$

(b) $n_p = 1.5$, $g = 0.9374$

Figure A.1 Examples of computed Mie scattering phase functions, for various particle refractive index. Images created with the website: https://multi-scattering.com/. The linear plots are on the left, the log scale plots are on the right. $\lambda = 600$ nm, $d = 1$ μm and $n_r = 1.3315$.
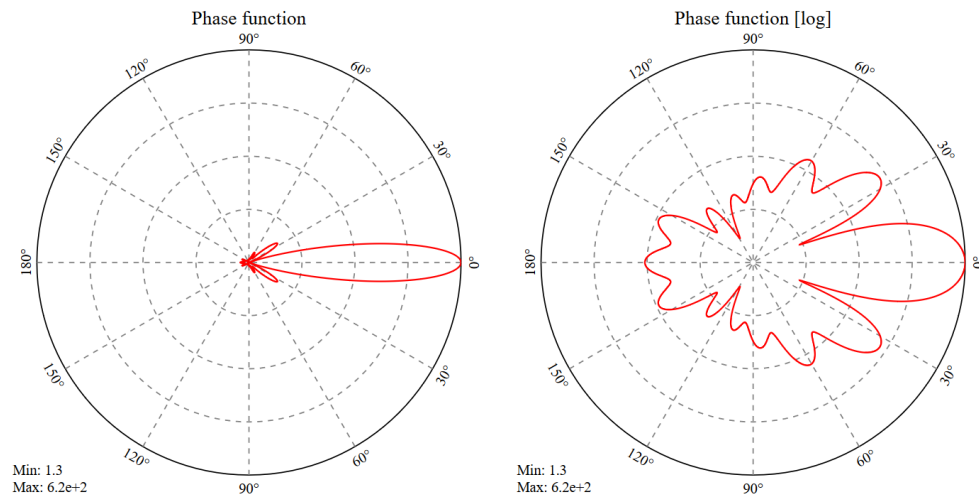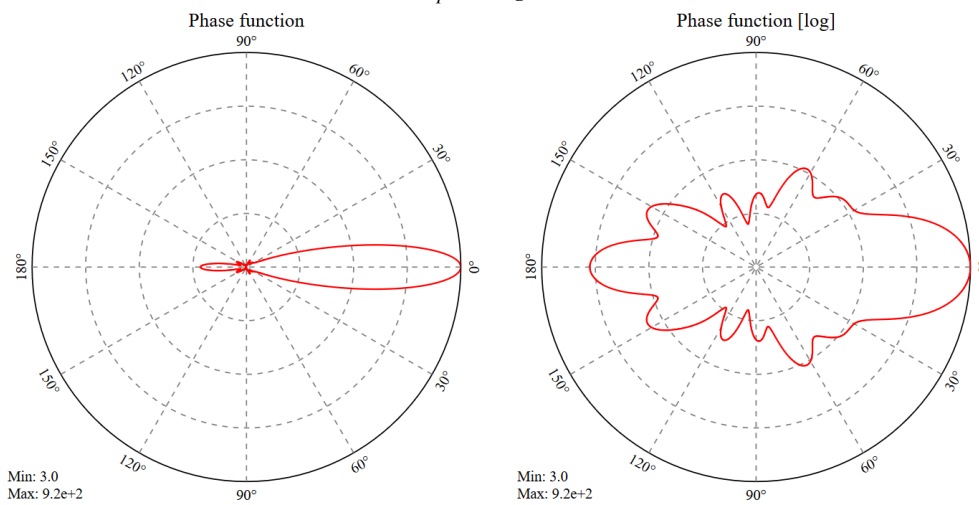
.

(a) $n_p = 2$, $g = 0.52$

(b) $n_p = 4$, $g = 0.4035$

Figure A.2 Examples of computed Mie scattering phase functions, for various particle refractive index. Images created with the website: https://multi-scattering.com/. The linear plots are on the left, the log scale plots are on the right. $\lambda = 600$ nm, $d = 1$ μm and $n_r = 1.3315$.

.

Appendix B

Fourier plane measurement of the phase function

Phase function is one of the key components in this thesis. As mentioned before, multiple Monte Carlo programs have already been created. Most of them don't incorporate the correct Mie scattering phase function and use the aproximated Henyey-Greenstein instead. This chapter will therefore explore a technique to extract the scattering phase function of the intralipids. The approach taken is to measure the phase function of intralipid in the Fourier plane. In this plane, the photons that escape from an object with the same angle will end up on a circle. The radius of the circle gets bigger with the angle. This means that by measuring the intensity of the light in the Fourier plane, the phase function can be reconstructed.

B.1   Method and setup

In Fourier optics, light enters a lens with an angle. All the light that enters with the same angle will be projected on the Fourier plane on a same distance r from the center. The Fourier plane is positioned at a focal length away from the lens. The angle-distance relationship can be represented in the following formula.

$$r = f tan(\theta) \tag{B.1}$$

Light comes from an object that scatters light into various directions. The lens was put as close as possible to the analysed object in order to catch all the photons escaped from it. Since the scattering phase function is symmetric, a setup that can cover $180°$ is sufficient. Moreover, since the particle size of the intralipids is comparable with the wavelength used, the scattering will be mostly forwards. It is estimated that a setup that covers $60°$ is acceptable.

In this experiment, laser light with two different wavelengths (473 nm and 532 nm) (Laserglow technologies, Toronto, Canada) is sent out to a sample of intralipid with $\tau = 1$. Since the optical depth is 1, most of the light will interact once with the particles and will be deviated according to the phase function. This light goes through a spherical lens and is projected on a sheet of paper in the Fourier plane. The sheet of paper has a pinhole in its center to let the non-interacting light pass. This is done to prevent a high intensity spot on the image and achieve better contrast. The projected light is then collected with a camera (Andor Zyla sCMOS, Oxford Instruments, Abingdon, United Kingdom) and further analysed. The full setup can be seen in figure B.1 and a closer look of the light scattering in the diluted intralipid is seen in figure B.2a, when intralipid is diluted to achieve OD =1.
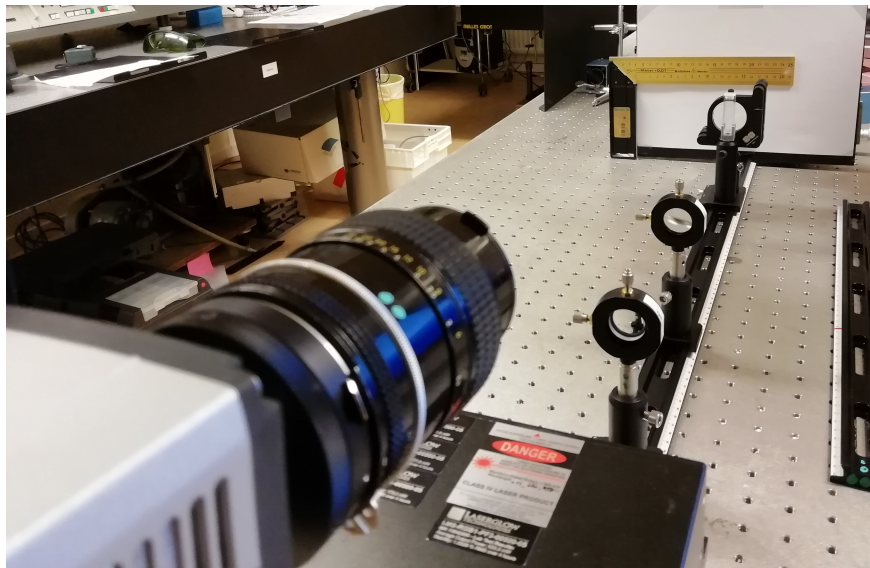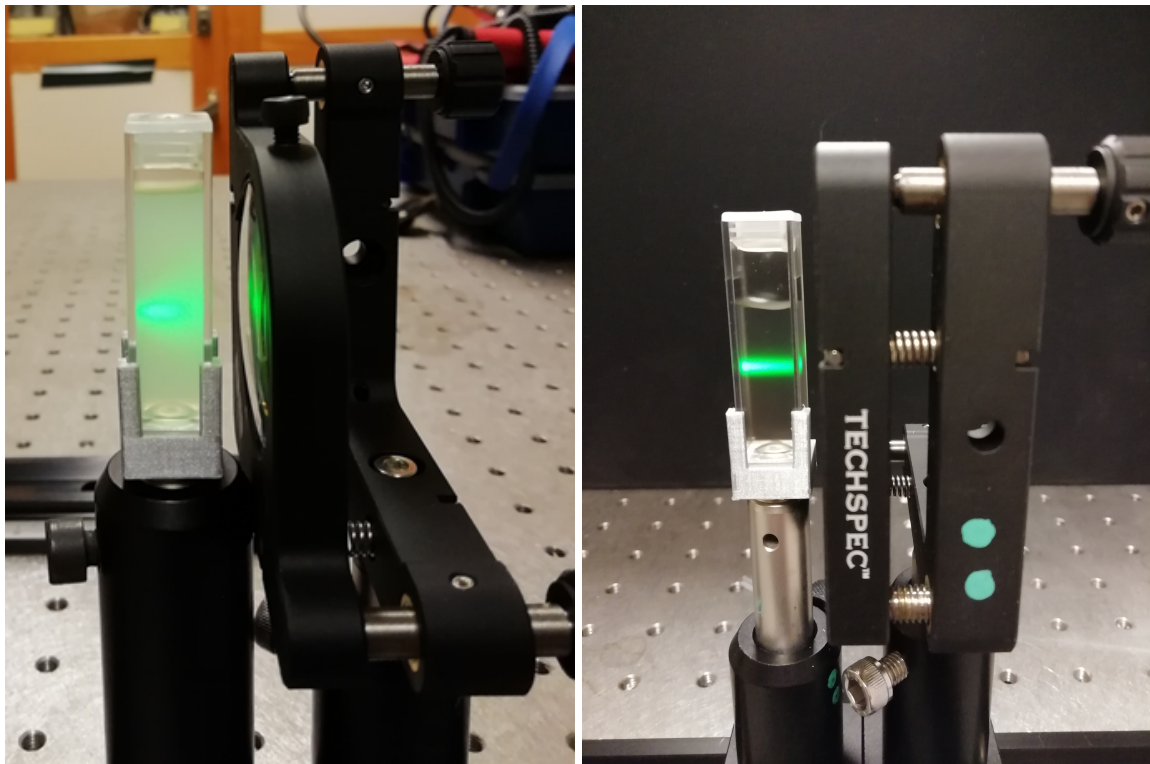

Figure B.1 Setup for the phase function measurement.

Figure B.2b shows us a closer look at an ink sample. Light escapes from the cuvette, which means that there is scattering in the ink and that the assumption we made is not completely true.

(a) Intralipid   (b) Ink

Figure B.2 Closer look at the cuvette and lens.

B.2 Results and discussion

The image of a known particle with diameter $4.94\mu m$ and of Intralipid 20% was taken. The images have been averaged into one intensity plot for better visualisation. The results are shown in figure B.3.
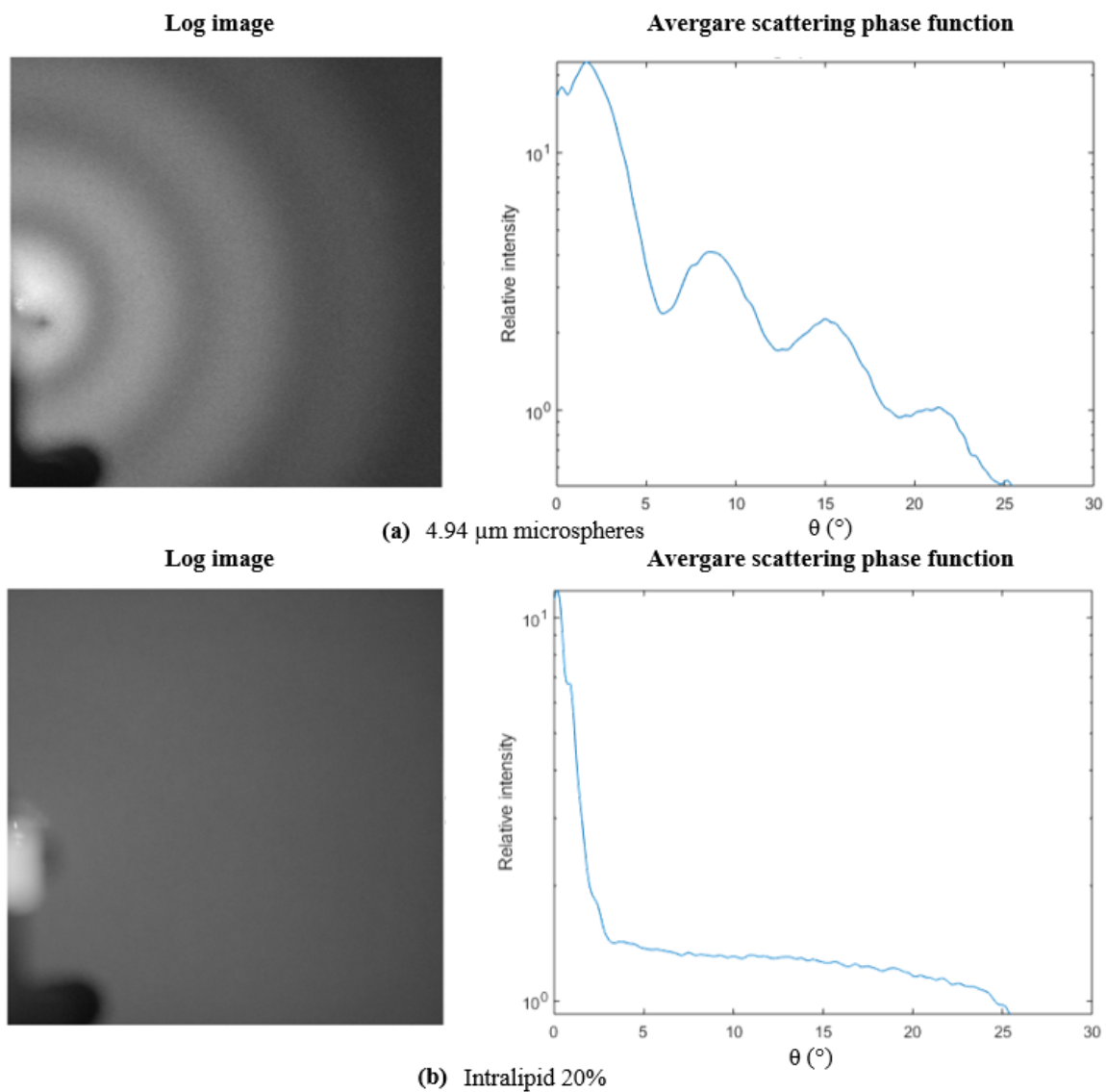
(a) 4.94 μm microspheres

(b) Intralipid 20%

Figure B.3 Setup for the phase function measurement.

In order to have an image like figure B.3.b, the particle size should be between 50 nm to 500 nm. The exact size and distribution are not known due to the many imperfections of the measurement.